

A 3D Model of the Local Bubble’s Magnetic Field: Insights from Dust and Starlight Polarization

THEO J. O’NEILL ¹, ALYSSA A. GOODMAN ¹, JUAN D. SOLER ², CATHERINE ZUCKER ¹ AND
JIWON JESSE HAN ¹

¹Center for Astrophysics | Harvard & Smithsonian, 60 Garden St., Cambridge, MA 02138, USA

²Istituto di Astrofisica e Planetologia Spaziali (IAPS). INAF. Via Fosso del Cavaliere 100, 00133 Roma, Italy

ABSTRACT

Clustered stellar feedback creates expanding voids in the magnetized interstellar medium known as superbubbles. Although theory suggests that superbubble expansion is influenced by interstellar magnetic fields, direct observational data on 3D superbubble magnetic field geometry is limited. The Sun’s location inside the Local Bubble provides a unique opportunity to infer a superbubble’s 3D magnetic field orientation, under the assumptions that: I) the Local Bubble’s surface is the primary contributor to plane-of-the-sky polarization observations across much of the sky, and II) the Local Bubble’s magnetic field is tangent to its dust-traced shell. In this work, we validate these assumptions and construct a model of the Local Bubble’s 3D B-field orientation from *Planck* 353 GHz polarization observations and a 3D-dust-derived model of the Local Bubble’s shell. We test Assumption I by examining correlations between the Local Bubble’s 3D geometry, dust polarization, and starlight polarization. We find that the Local Bubble likely dominates the polarized signal in the majority of lines of sight. We jointly test Assumptions I and II by applying our reconstruction method to a simulated superbubble, where we successfully reconstruct the 3D magnetic field orientation over the bulk of its surface. Finally, we use our 3D B-field model to infer the initial magnetic field orientation in the solar neighborhood prior to the Local Bubble’s formation, and derive an orientation parallel to the present-day Local Arm of the galaxy. These findings provide new insights into the co-evolution of superbubbles and the magnetized interstellar medium.

1. INTRODUCTION

Low-density cavities in the interstellar medium (ISM) generated by feedback from sequential supernovae are ubiquitous throughout the Milky Way (Heiles 1979; Pineda et al. 2023) and beyond (Watkins et al. 2023; Sandstrom et al. 2023). These “superbubbles” are expected to play a significant role in concentrating and distributing the effects of stellar feedback (Krumholz et al. 2014; Keller et al. 2014) and in triggering the formation of dense gas and stars (Elmegreen 2011; Dawson 2013). Although theoretical models and numerical simulations predict that the orientation of magnetic fields in the ISM has a significant impact on the direction of superbubble expansion (e.g., Ferriere et al. 1991; Tomisaka 1998; Ntormousi et al. 2017), the overall role of magnetic fields in regulating the formation, expansion, and interaction of superbubbles with their environment is unclear.

While 2D measurements of superbubble magnetic field orientation and strength have been obtained (e.g., Wisniewski et al. 2007; Gao et al. 2015; Thomson et al. 2018; Soler et al. 2018; Joubaud et al. 2019), efforts to map the 3D orientations of magnetic fields over the surfaces

of superbubbles have been limited by the uncertainties on their 3D geometries and by line-of-sight (LOS) confusion in the distances to structures contributing to the observed plane-of-the-sky (POS) B-field. Efforts to probe magnetic fields in 3D through the combination of POS and LOS tracers of B-field orientation have yielded rich insights into the effects of magnetic field structure on individual molecular clouds on the surface of superbubbles (Tahani et al. 2022a,b), but has so far remained out of reach over entire superbubble surfaces.

The Local Bubble is a superbubble centered roughly near the Sun’s present-day location (see reviews in Cox & Reynolds 1987; Welsh & Shelton 2009; Linsky & Redfield 2021). O’Neill et al. (2024) recently derived a new model of the Local Bubble’s dust-traced shell from 3D dust maps, revealing the Local Bubble as an irregular surface characterized by a prominent “chimney” in the high-latitude Northern hemisphere extending into the lower Galactic halo. The exact mechanisms regulating the Local Bubble’s formation and expansion into the disk and lower halo in the context of the magnetized ISM are not yet fully understood.

Magnetic fields have likely played a key role in determining the Local Bubble’s expansion. Past work studying local starlight polarization has revealed critical insights into the likely properties of the Local Bubble’s B-field (e.g., Heiles 1996; Santos et al. 2011; Berdyugin et al. 2014; Medan & Andersson 2019; Gontcharov & Mosenkov 2019), including that it likely makes a large contribution to the total observed sub-mm dust polarization at high latitudes (Skalidis & Pelgrims 2019). Alves et al. (2018) modeled magnetic fields on the surface of the Local Bubble at high Galactic latitudes ($|b| > 60^\circ$) with the simplifying assumption that the shell has an ellipsoidal geometry, and concluded that variations in the B-field in these polar regions would be sufficient to distort measurements of Galactic B-fields by a significant amount. Pelgrims et al. (2020) extended this work with a more physically motivated geometry (enabled by 3D dust mapping) to explore the initial orientation of the local Galactic Magnetic Field in the solar neighborhood. However, these efforts were also limited to the high-latitude regime.

A complete 3D model of the Local Bubble’s magnetic field structure over all latitudes would not only be a useful probe of the local history of the magnetized ISM, but also constrain variations between the local and larger-scale Galactic magnetic fields. In this work, we create the first complete 3D model of the Local Bubble’s magnetic field. Specifically, we constrain the Local Bubble’s magnetic field structure by combining its dust-traced surface geometry with *Planck* polarization observations and background starlight polarization measurements. We assume that: I) the observed POS magnetic field is primarily generated by a polarizing layer on the surface of the Local Bubble, and II) the 3D magnetic field is tangent to the surface of the Local Bubble. Combining these assumptions results in a complete set of 3D B-field vector orientations. This enables a full characterization of the B-field orientation over the Local Bubble’s surface to create the first 3D model of a superbubble’s magnetic field.

This paper is structured as follows. We describe the data used in our analysis in §2. We outline the geometric construction of the 3D B-field model from 2D polarization observations in §3. We explore various tests of Assumption I in §4 through analysis of starlight and sub-mm polarization observations. We explore tests of Assumption I and Assumption II in §5 by applying our B-field projection method to a simulated superbubble. We present our 3D model of the Local Bubble’s B-field in §6, which we use to model the initial orientation of the local Galactic magnetic field in the solar neighborhood before disruption by the Local Bubble. Finally, we dis-

cuss the implications of our work in §7 before concluding in §8.

2. DATA

2.1. Dust-traced Model of the Local Bubble

In this work, we make use of the O’Neill et al. (2024, hereafter O24) model of the Local Bubble’s dust-traced shell. This model was constructed from the Edenhofer et al. (2024) 3D map of dust extinction within 1.25 kpc of the Sun, which in turn was inferred from the Zhang et al. (2023) catalog of stellar distance and extinction estimates derived from *Gaia* BP/RP spectra.

The O24 model of the Local Bubble was constructed by identifying the Local Bubble’s shell as the first “significant” peak in differential extinction, A' , along the LOS from the Sun. The relative significance of a peak was defined using its prominence P (the height of a peak above its base). The inner and outer edges of peaks in the fiducial O24 model were defined by a half-prominence criterion ($A'_{0.5} = A'_{peak} - 0.5P$). O24 also defined a more generous one-tenth prominence model ($A'_{0.9}$) for shell width; we employ both of these boundary definitions at various times in this work. The model is sampled at HEALPix (Górski et al. 2005) $N_{\text{side}} = 256$ resolution.

Additional properties of the Local Bubble’s shell derived by O24 that we make use of in this work include: total extinction in *Gaia* G-band A_G , peak volume density of hydrogen n_{peak} (derived from A' by assuming a fixed ratio between extinction and hydrogen column density), the inclination of the shell to the POS γ , and the normal vector to the shell in cartesian space \mathbf{n} .

2.2. Planck Dust Polarization Observations

To constrain the B-field in the Local Bubble’s dust-traced shell, we used the component-separated 353 GHz Stokes I , Q , and U maps of Galactic dust polarization released as part of the 2018 Planck data release (Planck Collaboration et al. 2020b)¹ at uniform FWHM = 80’ resolution. The maps were produced using the Generalized Needlet Internal Linear Combination (GNILC) algorithm (Remazeilles et al. 2011) to separate foreground Galactic polarized thermal dust emission from polarized CMB emission (Planck Collaboration et al. 2020c), making these data appropriate for our study of nearby Galactic polarization.

We smoothed the maps to a full width at half maximum (FWHM) resolution of 2° . As a result of this generous smoothing, we do not perform any debiasing. Following Planck Collaboration et al. (2020c), we cor-

¹ COM_CompMap_IQU-thermaldust-gnilc-unires_2048_R3.00

rect intensity I for the cosmic infrared background ($-452 \mu\text{K}_{CMB}$) and Galactic zero level offset ($+63 \mu\text{K}_{CMB}$). We convert from K_{CMB} to MJy sr^{-1} using the unit conversion factor $287.5 \text{ MJy sr}^{-1} \text{ K}_{CMB}^{-1}$ (Planck Collaboration et al. 2020a). We downsample the map from its native resolution of HEALPix $N_{\text{side}} = 2048$ to $N_{\text{side}} = 256$ to match the angular spacing of the O'Neill et al. (2024) map of the Local Bubble.

We calculate polarized intensity as $P = \sqrt{Q^2 + U^2}$ and polarization fraction as $p = P/I$. We calculate polarization angle ϕ as

$$\phi = \frac{1}{2} \arctan(-U, Q), \quad (1)$$

following IAU convention, where angles are measured relative to the North Galactic Pole with positive values increasing with increasing Galactic latitude ℓ (Hamaker & Bregman 1996). The POS B-field orientation ψ_{\perp} can be inferred from ϕ as

$$\psi_{\perp} = \phi + \frac{\pi}{2}. \quad (2)$$

This stems from the assumption that, in the presence of an adequately strong B-field, the spinning, elongated dust grains in a given region of the ISM are likely to become preferentially aligned with their long axes perpendicular to the B-field. As a result, the thermal radiation emitting from these warm dust grains is polarized such that the observed ϕ is perpendicular to the POS component of the B-field ψ_{\perp} (see Andersson et al. 2015, for a review).

Our goal in this work is to infer the 3D B-field orientation \mathbf{B} , which will, by construction, appear identical to the pseudovector $\vec{\psi}_{\perp}$ when viewed in 2D projection on the POS.

2.3. Starlight Polarization Observations

Dust polarization observations (§2.2) yield the projected orientation of magnetic fields averaged over an entire LOS, but convey no direct information on distance to polarizing features. Optical polarimetry samples the LOS portion between the Sun and each star, providing additional information to resolve this ambiguity. To this end, we supplement the *Planck* dust polarization information with background starlight polarimetry observations, which allow us to constrain polarization as a function of distance from the Local Bubble's surface.

For this analysis, we identify the stars in the optical starlight polarization catalog assembled by Panopoulou et al. (2023) for which the Local Bubble contributes most of the integrated extinction along the LOS. To perform this cut, we restrict our analysis to stars with

median *Gaia* EDR3 photogeometric distances (Bailer-Jones et al. 2021) within the boundaries of the Edenhofer et al. (2024) 3D dust map, $d_{\star} < 1250 \text{ pc}$. We calculated the ratio of the integrated extinction from the Sun to the star, as defined in the Edenhofer et al. (2024) dust map, to the extinction from the Sun to the outer edge of the Local Bubble,

$$R_{\star} = \frac{A_{\star}}{A_{LB,outer}} = \frac{\sum_0^{d_{\star}} A_{ZGR23}}{\sum_0^{d_{LB,outer}} A_{ZGR23}} \quad (3)$$

We selected stars with $R_{\star} < 2$, i.e., stars whose foreground extinction are at most twice the extinction associated with the Local Bubble's interior and shell. We additionally excluded stars identified by the Panopoulou et al. (2023) catalog as possessing intrinsic polarization. Finally, we required all observations to have measurements of polarization fraction p , polarization fraction uncertainty e_p , and polarization angle ϕ , and exclude measurements with extremely low p ($p < 0.01\%$).

In total, this yielded a sample of 10,792 stars with polarization fraction and orientation measurements.² Distances from the Sun to the background stars in our sample range from $d = 7 - 1250 \text{ pc}$, encompassing stars both interior and exterior to the Local Bubble's surface.

Polarization fraction p is known to be a biased estimator of linear polarization strength. Following Panopoulou et al. (2023), we estimated debiased polarization fractions p_d as (Plaszczynski et al. 2014),

$$p_d = p - e_p^2 \frac{1 - e^{-p^2/e_p^2}}{2p}. \quad (4)$$

² The individual publications whose data were included in our analysis are, in order of number of measurements used: Heiles (2000); Franco & Alves (2015); Berdyugin et al. (2014); Santos et al. (2014, 2011); Pereyra & Magalhães (2004); Lobo Gomes et al. (2015); Panopoulou et al. (2015); Targon et al. (2011); Moneti et al. (1984); Vrba et al. (1976); Goodman et al. (1990); Berdyugin & Teerikorpi (2002); Alves & Franco (2007); Weitenbeck (2008); Berdyugin et al. (2001); Panopoulou et al. (2019b); Žejmo et al. (2017); Heyer et al. (1987); Vaillancourt et al. (2020); Alves & Franco (2006); Andersson & Potter (2010); Soam et al. (2015); Singh et al. (2022); Słowikowska et al. (2018); Oudmaijer et al. (2001); Berdyugin & Teerikorpi (2001); Neha et al. (2018); Soam et al. (2017); Alves et al. (2014); Eswaraiyah et al. (2011); Wang et al. (2017); Poidevin & Bastien (2006); Topasna et al. (2020); Santos et al. (2012); Andersson & Potter (2007); Whittet et al. (2001); Piirola et al. (2020); Eswaraiyah et al. (2019); Medhi et al. (2010); Cotton et al. (2019); Weitenbeck et al. (2008); Bailey et al. (2010); Panopoulou et al. (2019a); Alves et al. (2011); Gil-Hutton & Benavidez (2003); Soam et al. (2013); Sen et al. (2000); Eswaraiyah et al. (2013); Das et al. (2016); Cotton et al. (2017); Pereyra & Magalhães (2002); Choudhury et al. (2022); Bijas et al. (2022); Pandey et al. (2013); Andersson et al. (2013); Choudhury et al. (2019); Neha et al. (2016); Berdyugin et al. (2004); Chakraborty et al. (2014); Serón Navarrete et al. (2016).

Polarization angles ϕ in the Panopoulou et al. (2023) catalog are derived in an equatorial frame, increasing to the east from the North Celestial Pole and ranging between $[-90^\circ, 90^\circ]$. We converted the polarization angles to a Galactic frame, increasing to the east from the North Galactic Pole, following Stephens et al. (2011) (updated to a J2000 frame where the North Celestial Pole is located at $(\ell_n, b_n) = (122.93^\circ, 27.13^\circ)$). For a given measurement with declination δ and Galactic latitude ℓ , Galactic polarization angle ϕ_G can be derived from its equatorial polarization angle ϕ_E as

$$\phi_\star = \phi_G = \phi_E + \arcsin \left[\frac{\sin(\ell_n - \ell) \sin(90^\circ - b_n)}{\sin(90^\circ - \delta)} \right]. \quad (5)$$

We transform ϕ_\star so that $\phi_\star \in [0^\circ, 180^\circ]$.

As discussed in the previous subsection, the long axis of dust grains tends to be preferentially aligned perpendicular to the surrounding magnetic field. When initially unpolarized starlight encounters these aligned dust grains, a slightly larger fraction of the light will be blocked along the long axis of the grain than the short axis. This causes the starlight itself to become polarized, such that the overall measured polarization along the LOS towards the background star is the density-weighted average of polarization imparted by the dusty ISM along the LOS. Starlight polarization angles ϕ_\star are then parallel to the POS component of the B-field ψ_\star ,

$$\psi_\star = \phi_\star, \quad (6)$$

and can be compared directly to POS B-field orientations derived from dust polarization, ψ_\perp .

3. METHOD FOR RECONSTRUCTING 3D B-FIELD

3.1. Guiding Assumptions

We derived the Local Bubble’s 3D magnetic field orientation \mathbf{B} under the assumptions that:

- I. The Local Bubble’s surface is the last significant contributor to polarization measurements over most of the sky.
- II. \mathbf{B} is tangent to the dust-traced surface of the Local Bubble.

As we will discuss, we expect that both of these assumptions vary in accuracy and relevance over the surface of the Bubble.

Assumption I reflects our expectation that the low-density interior of the Local Bubble is unlikely to contain much polarizing material, meaning that, for emission originating at infinite distance and traveling towards the

solar system, the Bubble’s shell is likely the last significant source of polarization along the LOS. The Bubble’s interior has been observed to contribute relatively little polarization to background sources (e.g., Gontcharov & Mosenkov 2019), and the expanding shell is likely to make an oversized contribution to the total observed dust polarization, especially at intermediate to high latitudes (e.g., Skolidis & Pelgrims 2019). This behavior is borne out in simulations; e.g., Maconi et al. (2023) created synthetic 353 GHz dust polarization maps from an observer inside a Local Bubble-type cavity, and found that their simulated bubble acts as a polarizing “filter” over much of the simulated observer’s sky.

Assumption II stems from the theorized and observed behaviors of superbubbles interacting with magnetic fields. Simulations predict that in the process of a feedback-driven bubble’s expansion (whether that feedback is supernova-driven on the scale of superbubbles, or stellar wind-driven on the scale of HII regions), gas, dust, and magnetic fields in the surrounding ISM will be swept up into the bubble’s shell, yielding magnetic fields that are tangent to the bubble’s surface (Ferriere et al. 1991; Tomisaka 1998; de Avillez & Breitschwerdt 2005; Stil et al. 2009; van Marle et al. 2015; Ntormousi et al. 2017). This behavior is held out in 2D observations of bubbles; bubble-like morphologies are frequently traced by tangent magnetic fields (e.g., Soler et al. 2018; Bracco et al. 2020; Tahani et al. 2023). In their previous studies of the Local Bubble’s magnetic field, Alves et al. (2018) and Pelgrims et al. (2020) made this assumption of tangency while modeling the B-field at polar latitudes ($|b| \geq 60^\circ$).

We expect that Assumption I will be least reliable at low latitudes, i.e., in the Galactic plane where more confusion exists along the line of sight, and for LOS overlapping with low-density regions of the the Local Bubble’s shell. We expect that the geometrical constraint imposed by Assumption II will be least reliable in low-density regions of the shell where uncertainties on shell inclination are high (O’Neill et al. 2024).

3.2. Geometric Construction

We adopt the geometry shown in Fig. 1 to unify the true, 3D orientation of the magnetic field \mathbf{B} with its observed, 2D orientation projected into the POS. In this scenario, an observer within a magnetized bubble observes a 2D POS polarization orientation ϕ that translates to a (perpendicular) 2D B-field pseudovector $\vec{\psi}_\perp$. This pseudovector is a 2D projection (in Galactic coordinates, in the POS) of the true 3D vector \mathbf{B} . Assumption II ensures that there is only one possible 3D vector orientation

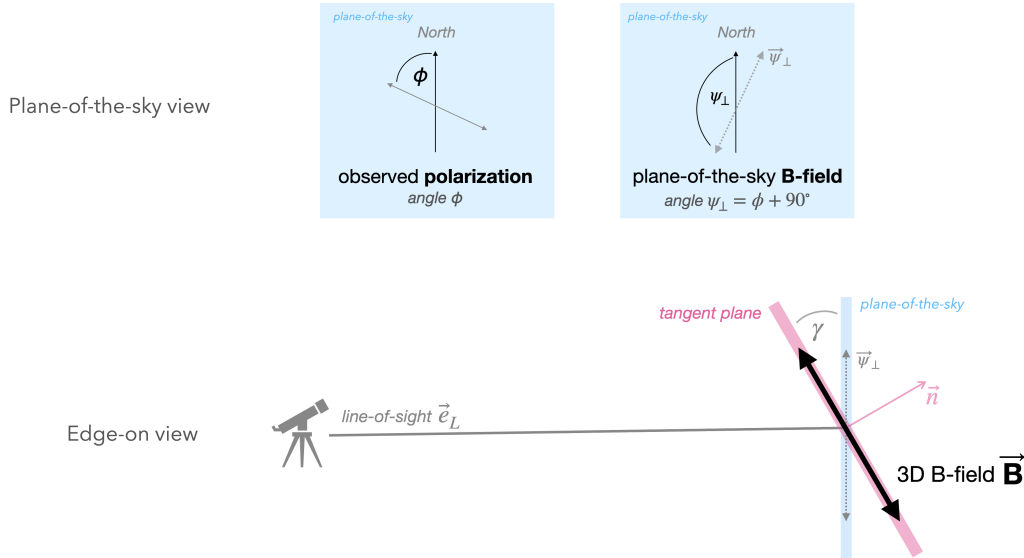


Figure 1. A schematic diagram showing the relationship between 2D and 3D magnetic fields adopted in this work. *Top row:* Plane-of-the-sky views (marked by blue squares) of an observed dust polarization vector (left, solid gray vector) and inferred B-field vector (right, dotted gray vector). *Bottom row:* An edge-on view of the adopted 3D geometry of the Local Bubble’s B-field. The 3D magnetic field (solid black vector) is constrained to the tangent plane to the Local Bubble’s surface (thick pink line). That vector projects to the 2D vector $\vec{\psi}_\perp$ (dashed gray vector) observed in the plane-of-the-sky (thick blue line). The tangent plane is inclined with respect to the plane-of-the-sky by angle γ , and is characterized by its normal vector \mathbf{n} (pink vector).

tation that could create that projected 2D pseudovector that in 3D space lies within the Bubble’s tangent plane.

We can describe this situation mathematically as follows. Our 3D B-field is defined in a Cartesian coordinate system,

$$\mathbf{B}(x, y, z) = (B_x, B_y, B_z), \quad (7)$$

with x pointing from the Sun towards the Galactic center at $\ell = 0^\circ$ [$\mathbf{B} = (1, 0, 0)$], y towards $\ell = 90^\circ$ [$\mathbf{B} = (0, 1, 0)$], and z towards the North Galactic Pole at $b = 90^\circ$ [$\mathbf{B} = (0, 0, 1)$].³

For each point on the Local Bubble’s surface, we define the LOS as a unit vector from the Sun to the point,

$$\mathbf{e}_L = \left(\frac{x}{d}, \frac{y}{d}, \frac{z}{d} \right), \quad (8)$$

where $d = (x^2 + y^2 + z^2)^{1/2}$. The tangent plane to each point on the Local Bubble’s surface was fit by O24 and is defined by its normal unit vector,

$$\mathbf{n} = (n_x, n_y, n_z). \quad (9)$$

Since \mathbf{e}_L is the normal vector to the POS, the angle between the POS and the tangent plane to the Local

Bubble’s surface can be defined as,

$$\gamma = \arccos(\mathbf{n} \cdot \mathbf{e}_L), \quad \gamma \in [0^\circ, 90^\circ]. \quad (10)$$

Under Assumption II, this is also the angle between the POS and the 3D B-field.

We matched LOS in the O24 Local Bubble model and the *Planck* measurements to assign a projected B-field angle ψ_\perp to each point on the Bubble’s surface. We then created a small offset from (ℓ, b) in the direction of $\vec{\psi}_\perp$ to define a new position $(\Delta\ell, \Delta b)$ in the POS along the projected orientation of the 2D B-field,⁴

$$\begin{aligned} \Delta\ell &= \ell + B_{\perp\ell}(\psi_\perp) \\ \Delta b &= b + B_{\perp b}(\psi_\perp). \end{aligned} \quad (12)$$

We transformed the offset 2D coordinates $(\Delta\ell, \Delta b)$ back to 3D Cartesian coordinates, and defined a unit vector

⁴ For a sufficiently small separation s , the offsets are *almost* equivalent to:

$$\begin{aligned} B_{\perp\ell} &= \sin(\psi_\perp)/s = \cos(\phi)/s \\ B_{\perp b} &= \cos(\psi_\perp)/s = -\sin(\phi)/s. \end{aligned} \quad (11)$$

However, to account for the effects of spherical geometry, we calculated $(B_{\perp\ell}, B_{\perp b})$ using the astropy function `directional_offset_by` (Astropy Collaboration et al. 2018).

³ Unless otherwise specified, all vectors \mathbf{v} reported in this work are unit vectors ($|\mathbf{v}| = 1$).

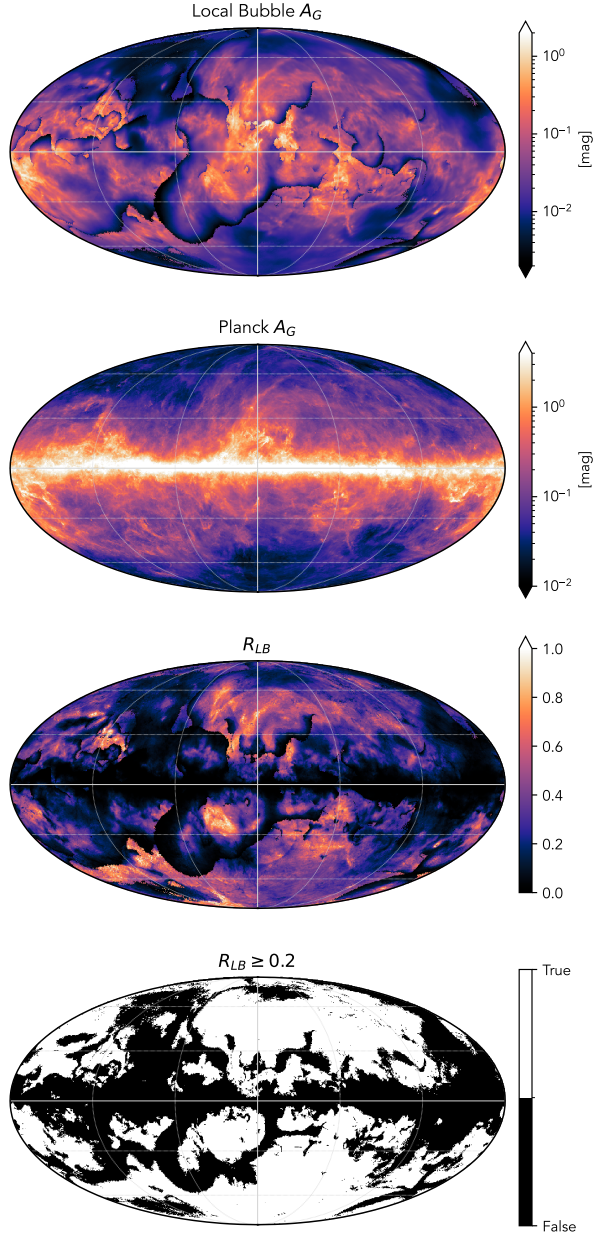


Figure 2. *Top:* Integrated dust extinction contributed by the O’Neill et al. (2024) model of the Local Bubble’s shell, $A_{G, LB}$. *Second from Top:* Estimated total extinction derived from the Planck Collaboration et al. (2016b) GNILC map of Galactic foreground reddening, $A_{G, Planck}$. *Third from Top:* Ratio, R_{LB} , of $A_{G, LB}$ to $A_{G, Planck}$. *Bottom:* Binary mask of regions with $R_{LB} \geq 0.2$, with regions passing this criterion shown in white. All panels are shown as all-sky Mollweide projections centered on the Galactic center.

from the Sun to the 3D offset,

$$\Delta \mathbf{B}_{\perp}(\psi_{\perp}) = (\cos \Delta \ell \cos \Delta b, \sin \Delta \ell \cos \Delta b, \sin \Delta b). \quad (13)$$

We can then define the 3D B-field \mathbf{B} as the normal to the plane containing both 1) the normal to the Local Bubble surface \mathbf{n} and 2) the normal to the plane containing \mathbf{e}_L and $\Delta \mathbf{B}_{\perp}(\psi_{\perp})$,

$$\mathbf{B} = \mathbf{B}(\mathbf{n}, \psi_{\perp}) = \frac{\mathbf{n} \times (\Delta \mathbf{B}_{\perp} \times \mathbf{e}_L)}{|\mathbf{n} \times (\Delta \mathbf{B}_{\perp} \times \mathbf{e}_L)|}, \quad (14)$$

i.e., as a unit vector at the intersection of the Local Bubble’s tangent plane and the projection of ψ_{\perp} into the POS. In other words, under Assumptions I and II, \mathbf{B} is the 3D magnetic field orientation on the surface of the Local Bubble.

4. ASSUMPTION I: THE LOCAL BUBBLE AS THE LAST SIGNIFICANT CONTRIBUTOR TO POLARIZATION METRICS

If Assumption I holds, we might expect the properties of the Local Bubble’s shell to affect the amount and orientation of polarization in the *Planck* 353 GHz maps and in background starlight polarization observations. In this section, we explore various correlations between the Local Bubble and *Planck* (§4.1) and starlight (§4.2) polarization.

4.1. Signatures of the Local Bubble in Planck Polarization Metrics

In this section, we analyze correlations between the Local Bubble’s 3D surface and 2D *Planck* polarization metrics: total intensity I , polarized intensity $P = \sqrt{Q^2 + U^2}$, and polarization fraction $p = P/I$. We adopt a simple model for total signal in the *Planck* maps as the sum of the signal from the Local Bubble and the “background”, defined as all emission from the volume beyond the Local Bubble’s surface),

$$\begin{aligned} I_{tot} &= I_{LB} + I_{bkg} \\ Q_{tot} &= Q_{LB} + Q_{bkg} \\ U_{tot} &= U_{LB} + U_{bkg}. \end{aligned} \quad (15)$$

Following the derivation of Planck Collaboration et al. (2015b) (which builds on the work of Lee & Draine 1985; Wardle & Konigl 1990, and others) for polarization parameters integrated along the LOS (parameterized here by dL), we can consider emission from the Local Bub-

ble's surface as being described by,

$$\begin{aligned}
 I_{LB} &= \int n_{LB} \beta [1 - p_0 (\cos^2(\gamma_{LB}) - 2/3)] dL \\
 Q_{LB} &= \int n_{LB} \beta p_0 \cos^2(\gamma_{LB}) \cos(2\phi_{LB,HPX}) dL \\
 U_{LB} &= \int n_{LB} \beta p_0 \cos^2(\gamma_{LB}) \sin(2\phi_{LB,HPX}) dL \quad (16) \\
 P_{LB} &= \int n_{LB} \beta p_0 \cos^2(\gamma_{LB}) dL \\
 p_{LB} &= \frac{p_0 \cos^2(\gamma_{LB})}{[1 - p_0 (\cos^2(\gamma_{LB}) - 2/3)]},
 \end{aligned}$$

where n_{LB} is the volume density of hydrogen in the Local Bubble's shell, γ_{LB} is the inclination of the Local Bubble's B-field to the POS, $\phi_{LB,HPX}$ is the Local Bubble's B-field's polarization angle in HEALPix convention (as opposed to the IAU convention used in the rest of this work), and p_0 is a factor related to the intrinsic polarization fraction and average dust grain geometry. For convenience, we have defined $\beta = \sigma_H B_\nu(T)$, where σ_H is the average dust cross section per hydrogen atom at 353 GHz and $B_\nu(T)$ is the Planck function at 353 GHz and temperature T .

We are interested in testing correlations that exist between these properties while holding β and p_0 constant. If we assume that γ_{LB} and $\phi_{LB,HPX}$ are constant along each LOS within the Local Bubble's shell, the integrals listed above reduce to a list of constants multiplied by $\int n_{LB} dL = N_H$, which would be easily obtained from the O24 model's integrated extinction within each LOS of the shell by assuming a fixed conversion between extinction and column density. However, since the integrated density of the shell strongly depends on the convention used to define its boundaries (e.g., $A'_{0.5}$ vs $A'_{0.9}$), we prefer to consider only the peak density of dust within each LOS, n_{peak} , which is invariant under shell definition convention.

In terms of testable predictions, we then investigate the following correlations:

$$\begin{aligned}
 I &\propto n_{peak} \\
 P &\propto n_{peak} \\
 I/n_{peak} &\propto [1 - p_0 (\cos^2(\gamma_{LB}) - 2/3)] \\
 P/n_{peak} &\propto \cos^2(\gamma_{LB}) \\
 p &\propto \frac{\cos^2(\gamma_{LB})}{[1 - p_0 (\cos^2(\gamma_{LB}) - 2/3)]}.
 \end{aligned} \quad (17)$$

We adopt a uniform value of $p_0 = 0.2$ (Planck Collaboration et al. 2015b) but verify that the derived correlation coefficients are insensitive to this choice.

Under the formulation of Eqn. 15, for quantities dependent on density (e.g., I) we expect the total signal

to be dominated by the Local Bubble in LOS where the integrated extinction of the Local Bubble's shell is a significant fraction of the integrated extinction of the background signal. In other words, we can consider the ratio of extinction from the Local Bubble's shell to total extinction along the LOS,

$$R_{LB} = \frac{A_{LB}}{A_{tot}} = \frac{A_{LB}}{A_{LB} + A_{bkg}}, \quad (18)$$

as a proxy for LOS where we expect to have the best chance of detecting the correlations outlined in Eqn. 17 in the *Planck* maps.

The extinction of the Local Bubble shell in *Gaia* G-band $A_{G,LB}$ was derived by O'Neill et al. (2024) for multiple definitions of the inner and outer boundaries of the Local Bubble's shell; to encompass the bulk of the shell's dust, we use $A_{G,LB}$ derived for their supplementary definition of the shell at a 1/10th prominence criterion ($A'_{0.9}$). For total extinction along the LOS, we query the Planck Collaboration et al. (2016b) GNILC map of $E(B - V)$ using the python package `dustmaps` (Green 2018). We convert these reddening estimates to G-band extinction assuming a fixed reddening vector of $R_V = 3.1$ (Cardelli et al. 1989) and a ratio between G and V band extinctions of $A_V/A_G = 1.36$ (Zhang et al. 2023), leading to a final relationship $A_{G,tot} = 2.28E(B - V)$.

Figure 2 shows, in 2D Mollweide projections, the Local Bubble shell extinction A_{LB} , total *Planck* extinction $A_{tot} = A_{planck}$, and their ratio R_{LB} . We define a mask based on a minimum threshold of $R_{LB} \geq 0.2$ (the median of the all-sky distribution, equivalent to $A_{LB} \geq 0.25A_{bkg}$; this mask is also shown in Figure 2) within which to investigate correlations between *Planck* metrics and the Local Bubble. This mask largely excludes the Galactic plane, portions of the low-density Local Chimney, and the diffuse edges of higher-density clouds within the Local Bubble's shell.

4.1.1. Correlations with Shell Density

Our first quantitative inquiry is into correlations (or lack thereof) between peak Local Bubble shell density n_{peak} and *Planck* I , P , and p . As outlined in Eqn. 17, we expect positive correlations between n_{peak} , I , and P , and no correlation between n_{peak} and p . Two-dimensional histograms of these relationships (within our mask of $R_{LB} \geq 0.2$) are shown in Figure 3.

As expected, we observe a strong positive correlation between n_{peak} and I (Spearman $\rho_s = 0.92$, $p < 0.001$) and a strong positive correlation between n_{peak} and P ($\rho_s = 0.77$, $p < 0.001$). These results are not terribly surprising: as the LOS passes through more dense material, intensity and polarized intensity both increase

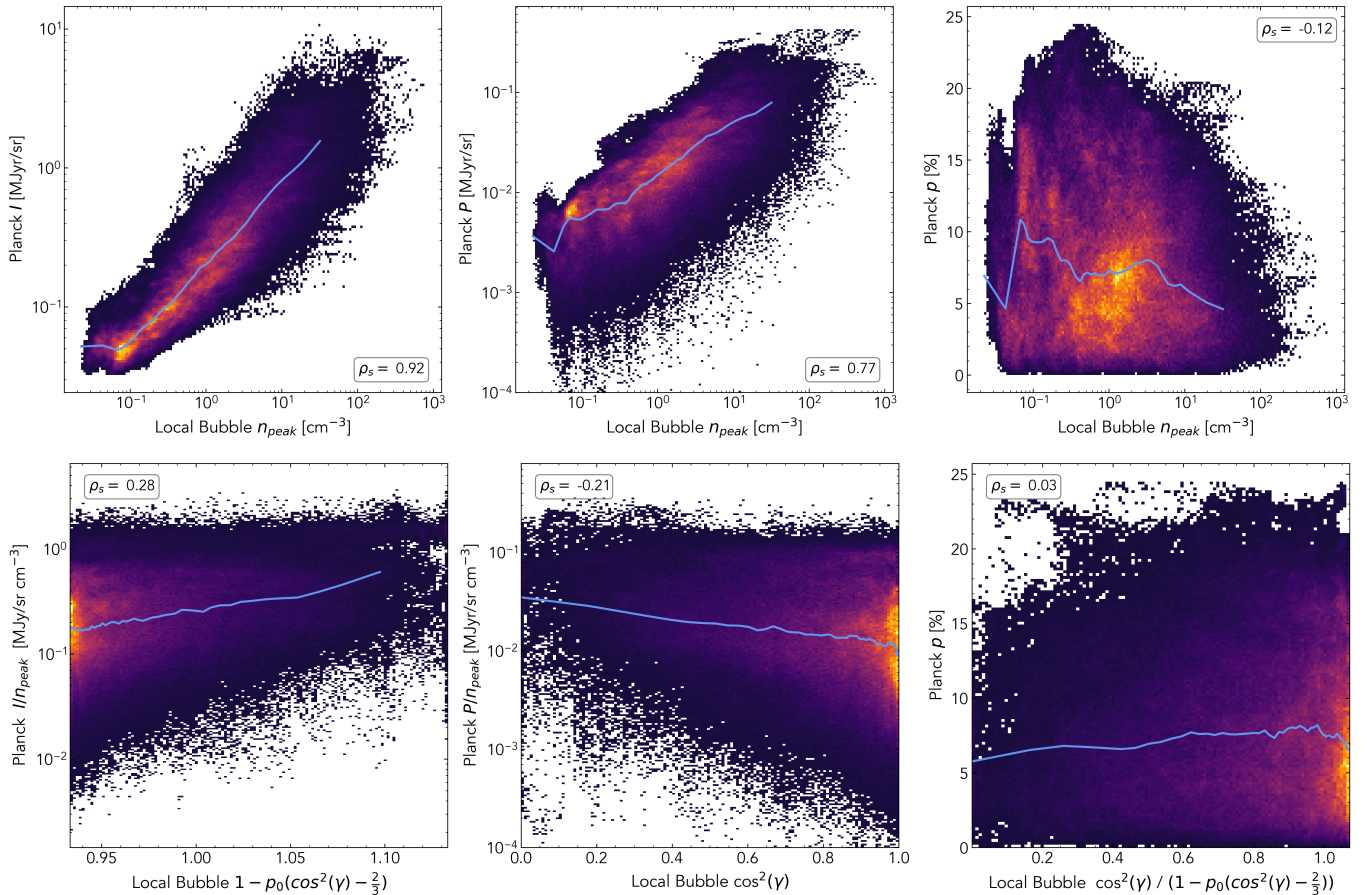


Figure 3. 2D histograms showing the relationship between *Planck* polarization metrics and properties of the Local Bubble’s shell, in the subset of LOS with $R_{LB} \geq 0.2$. *Top row:* Peak Local Bubble shell density n_{peak} vs. (from left) *Planck* I , P , and p . *Bottom row:* Terms dependent on Local Bubble shell inclination to the POS, γ , vs. (from left) I/n_{peak} , P/n_{peak} , and p . In each figure, the blue line shows the mean value of the independent variable as a function of the dependent variable. Spearman correlation coefficients ρ_s are reported in inset text boxes.

proportionally to the LOS density. There is a negligible negative correlation between n_{peak} and p ($\rho_s = -0.12$, $p < 0.001$). The lack of a meaningful correlation here is expected under Eqn. 17. We note that the overall shape of this correlation is nearly identical to the previously reported correlations between p and total hydrogen column density N_H by [Planck Collaboration et al. \(2015a\)](#) and [Planck Collaboration et al. \(2020c\)](#); this is also unsurprising, as Local Bubble shell density directly contributes to total hydrogen column density along the LOS. The decrease in the maximum p for increasing N_H has previously been interpreted by [Planck Collaboration et al. \(2015b\)](#) and [Planck Collaboration et al. \(2015a\)](#) as the result of turbulence and depolarization driven by the presence of variably-polarized structures along the LOS.

4.1.2. Correlations with Shell Inclination

We next consider correlations between *Planck* metrics and the inclination of the Local Bubble’s shell to

the POS, γ . Figure 3 shows 2D histograms of the correlations between various terms dependent on γ with I/n_{peak} , P/n_{peak} , and p (as outlined in Eqn. 17).

As expected, a weak positive correlation exists between I/n_{peak} and $1 - p_0(\cos^2(\gamma) - \frac{2}{3})$ ($\rho_s = 0.28$, $p < 0.001$). In the reverse of our expectations, a weak negative correlation exists between P/n_{peak} and $\cos^2(\gamma)$ ($\rho_s = -0.21$, $p < 0.001$). Finally, no meaningful correlation exists between p and $\cos^2(\gamma)/(1 - p_0(\cos^2(\gamma) - \frac{2}{3}))$ ($\rho_s = 0.03$, $p < 0.001$) (although we note that the maximum p for a given γ -derived term increases with γ -derived term, as expected).

In Appendix B.3, we evaluate the same correlations outlined in Eqn. 17 for a simulated Local Bubble equivalent. We observe remarkably similar qualitative relationships and quantitative correlation strengths as to what we have found for the real Local Bubble. This includes the negative correlation between P/n_{peak} and the

γ term, and the lack of correlation between p and the γ term.

The strength of any correlation between γ and polarization metrics such as p will be significantly affected by factors such as turbulence and confusion along the LOS, which we cannot directly control for in our observational data. Halal et al. (2024) recently suggested that the inclination of the Local Bubble's shell to the LOS/POS has no significant effect on *Planck* 353 GHz polarization fraction (p), and that p is instead significantly influenced by the complexity of structures along a given LOS contributing to the total 3D dust distribution. They argued that the lack of a meaningful correlation between p and shell inclination (in both the Pelgrims et al. (2020) and O24 models of the Local Bubble) indicates that either Assumption I and/or Assumption II are not physically motivated. The lack of correlation between p and γ for the simulated Bubble that we analyze in this work (where our analysis indicates that Assumption I and Assumption II are met for the majority of LOS) suggests that the strength of the correlation between p and γ is not a meaningful predictor of 3D B-field orientation. Since the Halal et al. (2024) arguments are predicated on this correlation between p and γ , our results challenge their interpretation that the magnetic field is unlikely to be tangential to the Local Bubble's shell over an appreciable fraction of the surface.

4.2. Signatures of the Local Bubble in Starlight Polarization Metrics

We supplement our distance-unresolved *Planck*-dust polarization observations with distance-resolved starlight polarization observations, assembled by Panopoulou et al. (2023) and described in §2.3. Various studies of the nearby background starlight polarization measurements have found compelling associations between distance, polarization fraction, and polarization orientation, especially in the context of the Local Bubble (e.g., Leroy 1999; Santos et al. 2011; Medan & Andersson 2019; Gontcharov & Mosenkov 2019; Skalidis & Pelgrims 2019).

The O24 model of the Local Bubble allows us to directly identify which stars in the Panopoulou et al. (2023) catalog fall inside vs. outside of the Bubble's shell. We expect that LOS that terminate on stars in the Local Bubble's interior should not have polarization properties that correlate with properties of the Bubble's shell (as their light does not pass through the magnetized shell), and that LOS terminating inside vs. outside the shell should consequently have significantly different polarization properties. We define the shell's inner (d_{inner}) and outer boundaries (d_{outer}) using O24's

fiducial map at a prominence threshold of $A'_{0.5}$. Under this definition, 19.5% of the background stars are in the Local Bubble's interior ($d_{\star} < d_{inner}$), 7.4% are within the Local Bubble's shell ($d_{inner} \leq d_{\star} \leq d_{outer}$), and 73.1% are located beyond the Local Bubble's shell ($d_{\star} > d_{outer}$).

We use this information to obtain a distance-resolved view of the effects of the Local Bubble on two quantities: debiased starlight polarization fraction p_d , and starlight polarization angle relative to *Planck* B-field orientation,

$$\Delta\theta_{planck} = \frac{1}{n_{planck}} \sum_i^{n_{planck}} \left| \arctan \frac{|\vec{\Psi}_{\perp} \times \vec{\Psi}_{\star}|}{\vec{\Psi}_{\perp} \cdot \vec{\Psi}_{\star}} \right|, \quad (19)$$

where agreement is averaged over the $n_{planck} = 100$ nearest measurements of ψ_{\perp} in the *Planck* map (in 2D projection). This measure of vector agreement ranges between $\Delta\theta_{planck} \in [0^{\circ}, 90^{\circ}]$, with $\Delta\theta_{planck} = 0^{\circ}$ indicating parallel alignment and $\Delta\theta_{planck} = 90^{\circ}$ indicating perpendicular alignment.

4.2.1. Global Variations in Starlight Polarization Properties

We first consider the global distributions of p_d and $\Delta\theta_{planck}$ in the interior, shell, and exterior of the Local Bubble. Figure 4 shows p_d and $\Delta\theta_{planck}$ as functions of distance from the peak extinction surface of the Local Bubble. Clear separations exist between the distributions of these properties for the interior, shell, and exterior populations.

The median values of p_d for stars in the Bubble's interior, shell, and exterior are 0.06%, 0.14%, and 0.79%, respectively. The median values of $\Delta\theta_{planck}$ for stars in the interior, shell, and exterior are 37° , 26° , and 18° . One-sided Kolmogorov-Smirnov (K-S) tests indicate that stars outside the Bubble have significantly higher p_d and lower $\Delta\theta_{planck}$ than stars inside the Bubble ($p < 0.001$ for both). Similarly, stars in the Bubble's shell have higher p_d and lower $\Delta\theta_{planck}$ than interior stars ($p < 0.001$ for both). For both properties, the shell population serves as a bridge between the interior and exterior distributions.

These results suggest that the passage of light through the Bubble's magnetized shell has left significant imprints on starlight polarization observations, increasing polarization fraction and changing the orientation of starlight polarization angles towards agreement with *Planck*. This latter point suggests that over much of the sample, *Planck* polarization orientations are set by passage through the Bubble's magnetized shell, in agreement with our Assumption I.

We emphasize that significant scatter in both p_d and $\Delta\theta_{planck}$ still exists even in the more homogeneous ex-

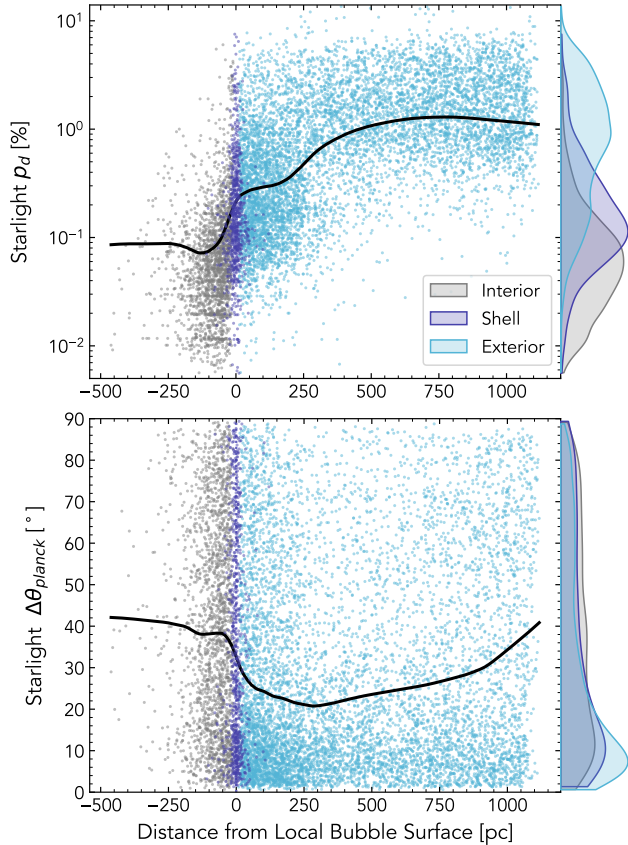


Figure 4. *Top:* Debiased starlight polarization fraction p_d as a function of stellar distance from the peak extinction surface of the Local Bubble. Background stars in the Local Bubble’s interior are marked in gray, while stars in the shell are shown in purple and stars exterior to the shell are shown in blue. The black line shows the average relationship between p_d and distance from the Local Bubble’s surface, smoothed with LOWESS regression (Locally Weighted Scatter-plot Smoothing, Cleveland 1979) with an inclusion fraction of 0.2. On the right edge of the figure, kernel density estimations of p_d are shown for each stellar distance group. *Bottom:* As top, but for starlight polarization orientation relative to *Planck* B-field orientation, $\Delta\theta_{planck}$.

terior sample. Additionally, the overall distribution of $\Delta\theta_{planck}$ peaks at a few degrees greater than $\Delta\theta_{planck} = 0^\circ$, suggesting a slight global offset between the starlight and 353 GHz orientations even in the exterior sample; potential causes of an overall offset between starlight and 353 GHz-derived B-field orientations were discussed in depth by Planck Collaboration et al. (2020c).

4.2.2. Local Variations in Starlight Polarization Properties

Significant variations may exist between LOS in the distributions of p_d and $\Delta\theta_{planck}$, particularly toward LOSs where these properties are the most affected by

the Bubble’s shell. In this section, we examine variations in p_d and $\Delta\theta_{planck}$ in specific regions of the sky.

To this end, we bin the sky into a HEALPix grid of $N_{side} = 2$, yielding 48 equal-area cells (each spanning roughly $29^\circ \times 29^\circ$). To include a cell in our analysis, we require that a minimum of 60 starlight LOS fall within the cell’s boundaries, of which at least 30 must terminate on background stars located within the Bubble’s interior and 30 within the Bubble’s exterior. We verify that our results are reasonably insensitive to the choice of minimum star count. We emphasize that each cell in this grid covers a relatively large area on-sky, and that the coverage of stars within each cell is not uniform.

With these requirements, 66.6% of the sky (31/48 cells) may be included in our experiments. Figure 5 shows p_d and $\Delta\theta_{planck}$ as a function of distance from Local Bubble’s surface for two of these cells; similar plots for all 31 cells analyzed are available online. Analysis of individual LOS reveals that, for the majority of cells, p_d increases when the surface of the Local Bubble is reached, and that $\Delta\theta_{planck}$ transforms from being relatively randomly distributed to clustering around low values (i.e., being parallel to the local *Planck* B-field orientation).

For each cell, we perform one-sided K-S tests between the interior and exterior starlight populations to test for significant differences in the distributions of p_d and $\Delta\theta_{planck}$ (with alternative hypotheses chosen to test for an increase in p_d and decrease in $\Delta\theta_{planck}$ in the exterior population). Figure 6 shows the results of these tests. At a significance threshold of p -value < 0.01 , 90.3% of cells have a significant increase in p_d outside the Local Bubble, and 54.9% have a significant decrease in $\Delta\theta_{planck}$. At a more generous threshold of $p < 0.05$, these values would increase to 100% for p_d and 64.52% for $\Delta\theta_{planck}$.

In the bottom panel of Figure 6, we overplot the centers of the considered cells on a map of the peak density of the Local Bubble’s shell, n_{peak} . For p_d , we observe that the three cells with no significant change are located along the low-density Northern Local Chimney identified by O24. For $\Delta\theta_{planck}$, cells with no difference are located along the Local Chimney as well as several other locations throughout the sky.

Figure 7 shows the correlation between the median properties of the Local Bubble’s shell in a cell (peak density n_{peak} and inclination γ) and the difference in the median value of p_d and $\Delta\theta_{planck}$ for starlight LOS ending within vs. outside the Local Bubble, which we

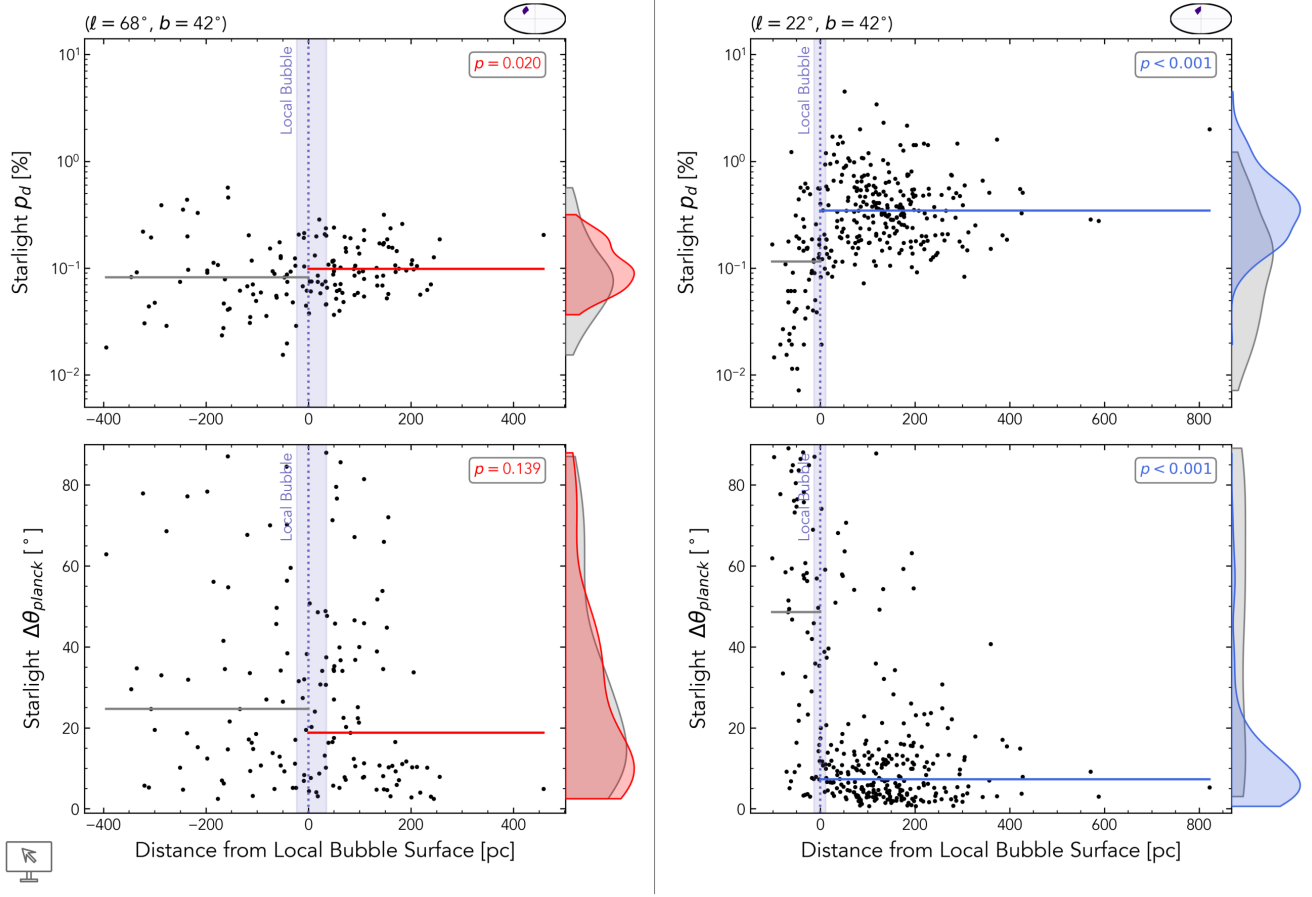


Figure 5. *Left and right:* As Figure 4, but for starlight polarization observations located along two distinct HEALPix $N_{\text{side}} = 2$ cells; the column on the left shows a cell where the Local Bubble’s shell has no significant effect on polarization percentage or orientation, while the column on the right shows a cell where both polarization percentage and orientation are significantly different inside vs. outside the Local Bubble’s shell. Central coordinates and on-sky location of the HEALPix cells are shown at the top of each figure. The average extent of the Local Bubble’s inner and outer edge within the cell is marked in purple. The median values of starlight polarization metrics inside vs. outside the Local Bubble’s surface are marked with horizontal lines. p -values for one-sided Kolmogorov Smirnov tests comparing the distribution of internal vs. external properties are reported in inset text boxes. If $p \geq 0.01$ (as is the case for the HEALPix cell on the left), the median line and KDE for the external starlight sample are colored in red; if $p < 0.01$ (as is the case on the right), they are colored in blue. A full figure set showing equivalent plots for all HEALPix cells analyzed is available online: https://theo-oneill.github.io/magneticlocalbubble/starlight_LOS/

define as

$$\begin{aligned} \delta p_d &= \text{med}(p_d[d \geq d_{LB}]) - \text{med}(p_d[d < d_{LB}]) \\ \delta \Delta \theta_{\text{planck}} &= \text{med}(\Delta \theta_p[d \geq d_{LB}]) - \text{med}(\Delta \theta_p[d < d_{LB}]). \end{aligned} \quad (20)$$

We find a strong positive correlation between n_{peak} and δp_d ($\rho_s = 0.81$), and a moderate negative correlation between n_{peak} and $\delta \Delta \theta_{\text{planck}}$ ($\rho_s = -0.38$). This suggests that higher-density regions of the Local Bubble’s shell create a larger imprint on polarization fraction and orientation. We find a very weak negative correlation between γ and δp_d ($\rho_s = -0.15$), and a moderate positive correlation between γ and $\delta \Delta \theta_{\text{planck}}$ ($\rho_s = 0.34$).

In summary, we find that starlight polarization measurements that sample portions of the LOS outside of

the Local Bubble have higher polarization fractions and are more aligned with the *Planck* B-field orientation than starlight polarization measurements that terminate on stars inside the Bubble. These effects are susceptible to position and shell density, with no significant differences originating along the low-density Local Chimney identified by O24. A decrease in $\Delta \theta_{\text{planck}}$ occurs even in large portions of the Galactic plane, where the ratio of extinction from the Local Bubble to total extinction along the LOS (R_{LB} , Figure 2) is extremely low — suggesting that even in these extremely confused LOS, *Planck* polarization orientation may still be dominated by passage through the last significant surface along the LOS, i.e., the Local Bubble, and that our Assumption I holds. These conclusions are limited by uneven spatial

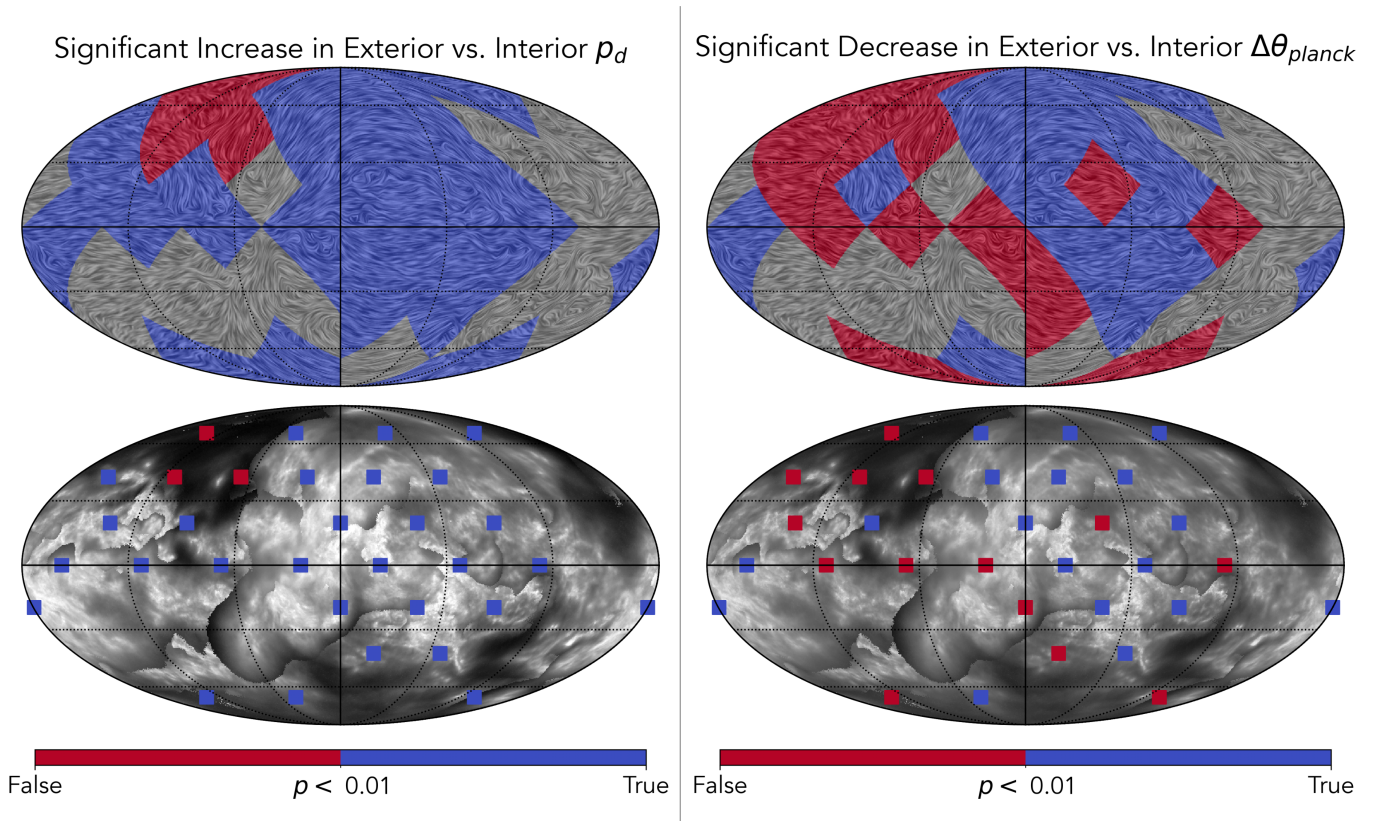


Figure 6. On-sky summary of the results of the starlight polarization significance testing demonstrated in Figure 5. *Top left:* HEALPix cells with a significant ($p < 0.01$) increase in p_d in the exterior starlight group are colored in blue (e.g., the $(\ell, b) = (22^\circ, 42^\circ)$ cell shown in the right column of Figure 5), while those with no significant increase are colored in red (e.g., the $(\ell, b) = (68^\circ, 42^\circ)$ cell shown in the left column of Figure 5). Cells with insufficient sampling of stars are colored in gray. A Line Integral Convolution of *Planck* B-field orientation is overlaid by the translucent drapery pattern. *Bottom left:* Scatter points marking the central coordinates of analyzed HEALPix cells, with colors as in the top panel, are overlaid on a grayscale map of peak Local Bubble shell density. *Top right and Bottom right:* As left, but for a significant decrease in starlight polarization angle relative to *Planck*, $\Delta\theta_{planck}$.

sampling of starlight polarization measurements inside and outside of the Local Bubble; a more uniform and much more extensive catalog of background polarization measurements would be needed to probe these effects at smaller angular scales.

5. ASSUMPTION II: TANGENCY OF THE LOCAL BUBBLE’S B-FIELD AND SHELL

We now consider the second guiding assumption of this work: that the Local Bubble’s 3D B-field is tangent to its dust-traced shell. Directly testing this theoretically-predicted result is not possible with current datasets; we must instead turn to simulations of superbubbles expanding into a magnetized ISM to probe this assumption.

To this end, we apply our B-field projection method (§3.2) to synthetic polarization maps created by Maconi et al. (2023, hereafter M23) for an observer in the interior of a simulated superbubble analogous to the Local Bubble. We then compare the true orientation of the 3D

B-field at the simulated bubble’s surface with the projected 3D B-field inferred from our projection method. We describe our results in full in Appendix B, and refer the interested reader to that section for a complete description of our methods and results. Here, we highlight the main takeaways of this analysis that may be applicable to our observed Local Bubble.

As reported in Appendix B.2, we first test Assumption II alone by measuring the difference in orientation between the true 3D B-field in the simulated superbubble’s shell and the normal vector to the simulated shell. We find that the true 3D B-field is significantly closer to tangent to the simulated Bubble’s surface than a random field, and falls within 40° of tangency for 91% of simulated LOS on the Bubble’s surface (where 40° is the $+2\sigma$ quantile of the distribution of vector orientation uncertainties for the observed Local Bubble, as derived in Appendix A). This indicates that Assumption II is generally well-motivated over the majority of the

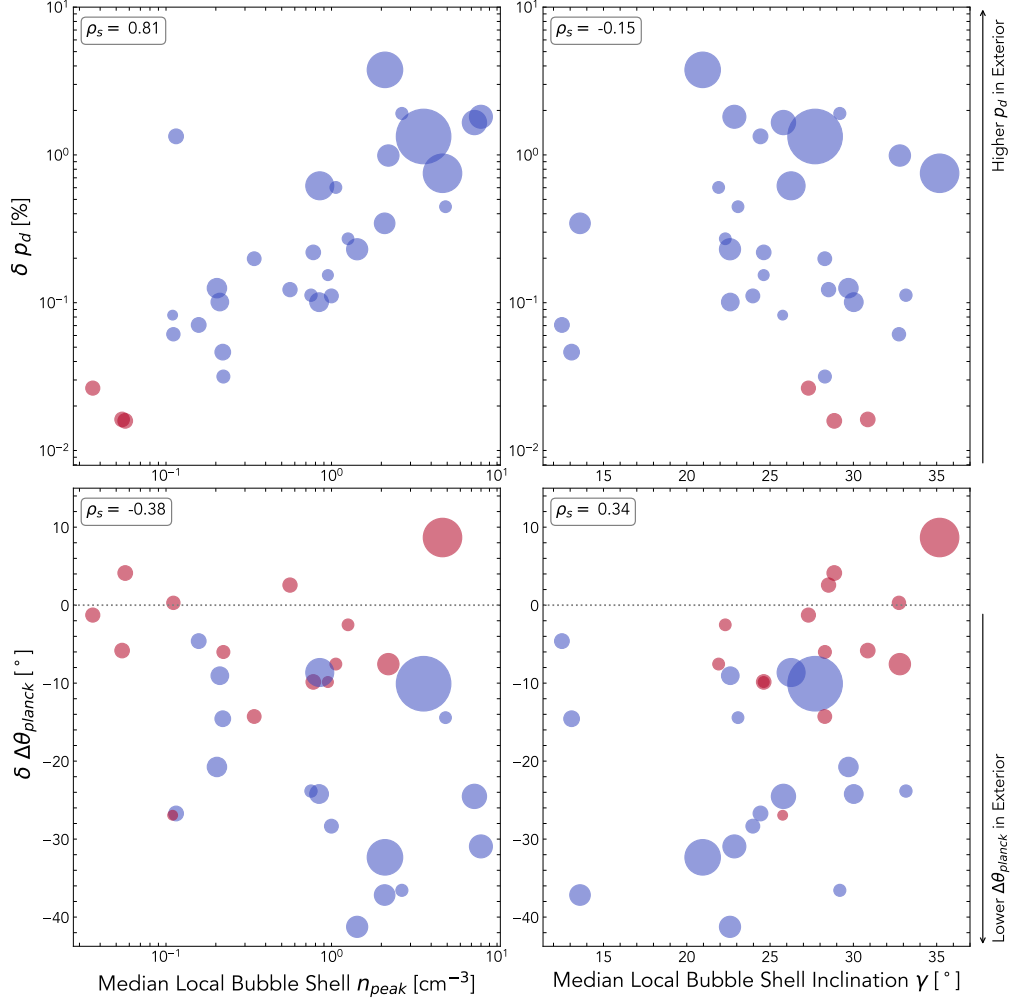


Figure 7. Relationships between properties of the Local Bubble’s shell and the difference in median starlight polarization properties inside vs. outside the Local Bubble, for the HEALPix cells analyzed in Figure 5, are displayed. *Top left:* Change in starlight polarization fraction δp_d vs. median Local Bubble shell density n_{peak} . *Top right:* δp_d vs. median Local Bubble shell inclination γ . *Bottom left:* Change in starlight polarization orientation relative to *Planck* $\delta\Delta\theta_{planck}$ vs. n_{peak} . *Bottom right:* $\delta\Delta\theta_{planck}$ vs. γ . In all figures, points are sized proportionally to the number of stars in the HEALPix cell. They are colored according to the results of their K-S tests (with blue marking significant differences). Spearman correlation coefficients ρ_s are displayed in the inset text boxes.

simulated bubble’s surface. A weak negative correlation exists between tangent orientation and dust density.

We then test the combination of Assumption I and Assumption II by measuring the difference in orientation between the true 3D B-field and the projected 3D B-field. We observe that the true 3D B-field’s orientation is significantly closer to parallel to the projected 3D B-field than a random field, and falls within 40° of parallel orientation for 60% of simulated LOS on the Bubble’s surface. This suggests that the combination of Assumption I and Assumption II is well-motivated for the simulated bubble. Weak correlations exist between parallel orientation, increasing B-field strength, and decreasing inclination to the POS.

In summary, Assumptions 1 and 2 appear well-motivated in the context of the simulated bubble. We conclude that applying these assumptions to the real Local Bubble can likely yield a reasonable model of its true 3D B-field.

6. MODELING THE LOCAL BUBBLE’S 3D MAGNETIC FIELD

Having established that our guiding assumptions are well-motivated, we now describe the results of projecting the 2D *Planck* polarization observations onto the 3D Local Bubble surface. We first describe several nuances in visualizing this 3D B-field (§6.1), and then report the mean orientation of the B-field in 3D space and in 2D Galactic projection (§6.2). Finally, we model the initial

orientation of the local Galactic Magnetic Field in the present-day solar neighborhood in §6.3.

6.1. Visualizing the 3D Model

Our primary visualization tool for the Local Bubble’s 3D B-field is a directionless vector field overlaid on the O24 model of the Local Bubble. For clarity, we defined a subsample of the full set of \mathbf{B} vectors spaced at ~ 10 pc intervals. The resulting 10 pc spacing vector field is shown in Figure 8. The underlying LB model is colored by distance from the Sun to the Local Bubble surface to aid with depth perception.

A machine-readable table of the full HEALPix $N_{\text{side}} = 256$ -spaced representation of the 3D B-field is available online. Since polarization data can only yield pseudovector orientation and not direction, an equivalency $(B_x, B_y, B_z) = (-B_x, -B_y, -B_z)$ holds for all 3D vectors. We also report uncertainties on vector orientation; we discuss our error estimation process in Appendix A.

6.2. Mean Orientation of the Present-Day 3D B-field

Alves et al. (2018, hereafter A18) and Pelgrims et al. (2020, hereafter P20) both previously modeled the Local Bubble’s magnetic field at high latitudes ($|b| \geq 60^\circ$) using *Planck* 353 GHz polarization maps. As part of their work, they provided summaries of the present-day orientation of the Local Bubble’s B-field in terms of the mean orientation towards Galactic coordinates (ℓ_B, b_B) . Here we present the mean 3D $(\bar{B}_x, \bar{B}_y, \bar{B}_z)$ and 2D (ℓ_B, b_B) orientations of our model of the Local Bubble’s B-field over various portions of the sky (including the $|b| \geq 60^\circ$ polar caps, for direct comparison to the results of A18 and P20).

We note that, since $\mathbf{B} = -\mathbf{B}$, simply taking the mean of the full distributions of the 3D B-field’s vector components would yield results biased towards the convention adopted for vector direction. To avoid this effect, we derive the mean 3D orientation $\bar{\mathbf{B}} = (\bar{B}_x, \bar{B}_y, \bar{B}_z)$ as the first eigenvector \mathbf{s}_1 of the scatter matrix, $\bar{\mathbf{S}} = \frac{1}{n} \sum_{i=1}^n \mathbf{B}_i \mathbf{B}_i^T$, a procedure which is appropriate for a Watson distribution of axially-symmetric unit vectors with concentration parameter $\kappa > 0$ (Mardia & Jupp 2000); see Appendix A for further discussion of the Watson distribution as applied to \mathbf{B} .

We provide a summary of these mean orientations in Table 1. A consequence of the lack of vector direction is that each (ℓ_B, b_B) corresponds to an equivalent $(\ell_B + 180^\circ, -b_B)$. We derive a global average $(\ell_B, b_B) = (61.7^\circ, 1.7^\circ)$ over the full sky, which remains relatively constant for the subset of LOS with $R_{LB} \geq 0.2$

$((\ell_B, b_B) = (63.4^\circ, 2.1^\circ))$. In the polar caps, ℓ_B tends to take similar values to the whole sky, while b_B obtains a significant vertical components; values for the Northern cap center on $(\ell_B, b_B) = (65.6^\circ, -13.2^\circ)$, and for the Southern on $(\ell_B, b_B) = (77.2^\circ, 7.0^\circ)$.

As summarized in Table 1, these orientations are in generally good agreement with P20’s results for (ℓ_B, b_B) in the polar caps; for their $l_{\text{max}} = 6$ model of the Local Bubble, P20 derived $(\ell_B, b_B) = (71^\circ, -10.9^\circ)$ and $(\ell_B, b_B) = (74^\circ, 5.8^\circ)$ for the North and South, respectively. The values derived by A18 $((\ell_B, b_B) = (70^\circ, 43^\circ)$ and $(\ell_B, b_B) = (74^\circ, -14^\circ)$ for the Northern and Southern caps, respectively) are similar in ℓ_B but dissimilar in b_B . We expect these differences are driven both by differences in choice of Local Bubble model and *Planck* data release and smoothing scale.

6.3. Initial Orientation of the Local Galactic Magnetic Field

In addition to measuring the mean present-day orientation of the Local Bubble’s B-field, A18 and P20 also modeled the initial orientation of the B-field in the solar neighborhood before disruption by the Local Bubble. This is possible under Assumption II and the assumption of pure radial expansion from a point in the interior of the Local Bubble, which together imply that the present-day orientation of the Local Bubble’s B-field encodes information about the initial orientation of the interstellar B-field. In this section, we infer this initial 3D orientation of the local component of the Galactic Magnetic Field (GMF) from our derived 3D model of the Local Bubble’s present-day B-field.

6.3.1. Mathematical Formulation of the Initial Magnetic Field

The local GMF \mathbf{B}_G can be modeled as consisting of a uniform component \mathbf{B}_0 and a turbulent component \mathbf{B}_T (Hildebrand et al. 2009; Planck Collaboration et al. 2016a),

$$\mathbf{B}_G = \mathbf{B}_0 + \mathbf{B}_T. \quad (21)$$

In this work, we focus on modeling \mathbf{B}_0 and neglect \mathbf{B}_T . We assume that the orientation of \mathbf{B}_0 was uniform at all points in 3D space in the solar neighborhood before the Local Bubble’s progenitor supernovae occurred,

$$\mathbf{B}_0(x, y, z) = (B_{x,0}, B_{y,0}, B_{z,0}). \quad (22)$$

As the Local Bubble expanded from (a) supernova(e) centered at 3D coordinates c_0 ,

$$c_0 = (x_0, y_0, z_0), \quad (23)$$

\mathbf{B}_0 would have been swept up into and become tangent to the Local Bubble’s shell (Assumption II). Using an

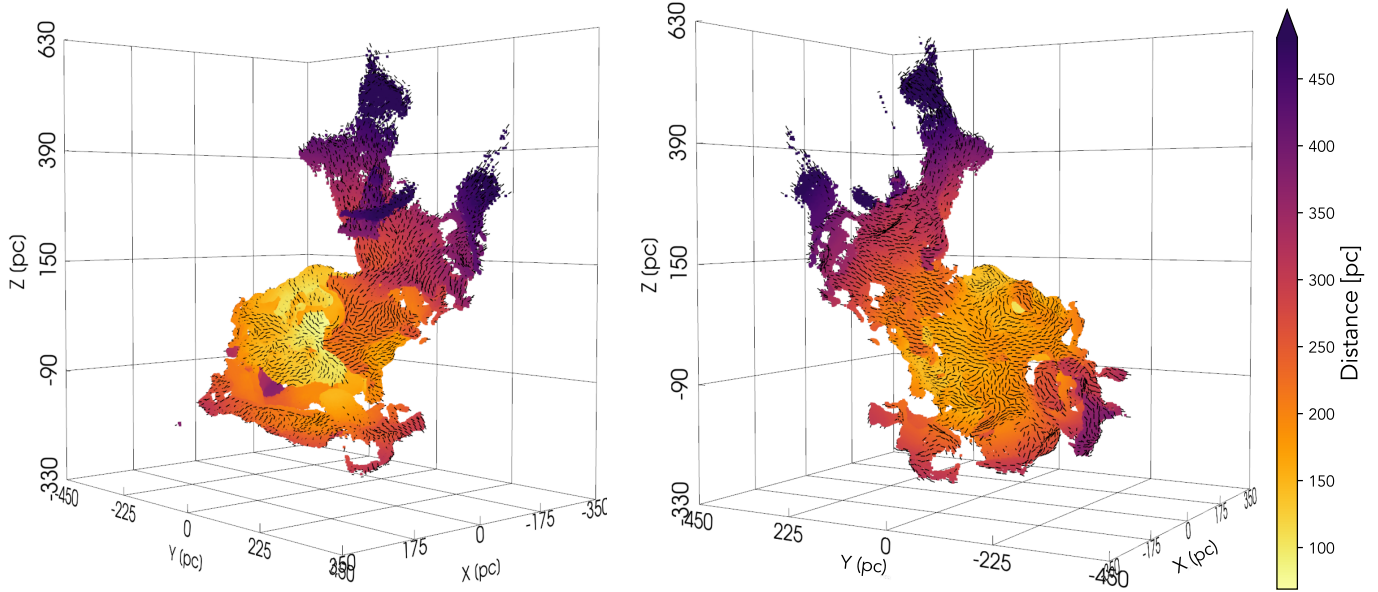


Figure 8. Two views of our 3D model of the Local Bubble’s magnetic field. The 3D B-field model is represented by black vectors overlaid on the O’Neill et al. (2024) model of the Local Bubble (colored by distance from the Sun). An interactive figure is available online: <https://theo-oneill.github.io/magneticlocalbubble/Bfield/>

Table 1. Mean Orientation of Local Bubble’s B-field

Region	% LOS	$(\bar{B}_x, \bar{B}_y, \bar{B}_z)$	$(\bar{\ell}_B, \bar{b}_B)$ [°]	P20 $(\bar{\ell}_B, \bar{b}_B)$ [°]	A18 $(\bar{\ell}_B, \bar{b}_B)$ [°]
All	(100%)	(0.474, 0.880, 0.030)	(61.7, 1.7)		
$R_{LB} \geq 0.2$	(52.2%)	(0.448, 0.893, 0.037)	(63.4, 2.1)		
Poles	(13.4%)	(0.309, 0.951, -0.015)	(72.0, -0.9)		
North	(6.7%)	(0.401, 0.887, -0.229)	(65.6, -13.2)	(71.0, -10.9)	(70, 43)
South	(6.7%)	(0.220, 0.968, 0.122)	(77.2, 7.0)	(74.0, 5.8)	(74, -14)

NOTE—% LOS reports the percentage of total lines-of-sight that are included in each region. Polar regions are defined as $|b| \geq 60^\circ$. $(\bar{\ell}_B, \bar{b}_B)$ reports the mean orientation of the B-field in 2D Galactic coordinates, compared to Pelgrims et al. (2020, P20) and Alves et al. (2018, A18).

approximation of the Local Bubble’s shell as very thin, A18 formulated the present-day B-field orientation on the Local Bubble’s shell as,

$$\mathbf{B}(\mathbf{r}) = \frac{r_0}{r} \frac{\partial r_0}{\partial r} \frac{1}{\mathbf{n} \cdot \mathbf{e}_r} [\mathbf{n} \times (\mathbf{B}_0 \times \mathbf{e}_r)], \quad (24)$$

where r_0 is the initial position of each particle swept up in the shell, r is the present day position of those particles, and \mathbf{e}_r is the radial basis vector originating from c_0 ,

$$\mathbf{e}_r = \left(\frac{x - x_0}{d_0}, \frac{y - y_0}{d_0}, \frac{z - z_0}{d_0} \right), \quad (25)$$

where $d_0 = ((x - x_0)^2 + (y - y_0)^2 + (z - z_0)^2)^{1/2}$. This formulation assumes that the direction of the Local Bubble’s expansion from c_0 has been solely radial (directed along \mathbf{e}_r). A18 and P20 both used this formulation to fit the initial orientation of \mathbf{B}_0 in 2D projection, where \mathbf{B}_0 can be considered as being oriented towards some coordinate pair (ℓ_0, b_0) . In this work, we extend A18 and P20’s 2D fitting to infer the initial 3D orientation of the B-field \mathbf{B}_0 and expansion center c_0 . Since we are only interested in present-day B-field orientation and not strength, we formulate the present-day modeled B-field

orientation \mathbf{B}_M as a unit vector,

$$\mathbf{B}_M = \frac{\mathbf{n} \times (\mathbf{B}_0 \times \mathbf{e}_r)}{|\mathbf{n} \times (\mathbf{B}_0 \times \mathbf{e}_r)|}. \quad (26)$$

We note that Equation 26 takes the same general form as our model for the observed present-day B-field (Equation 14).

6.3.2. Fitting Method

The orientation of \mathbf{B}_M is fully described by 9 parameters: the three cartesian components of the normal vector \mathbf{n} to the Local Bubble’s shell, the three components of the original 3D B-field \mathbf{B}_0 , and the center of radial expansion c_0 . O24 fit a tangent plane defined by the normal vector \mathbf{n} to each point on the Local Bubble’s surface. After considering these fit \mathbf{n} as givens, we are left with six free parameters θ to fit to describe \mathbf{B}_0 and c_0 ,

$$\theta = [B_{0x}, B_{0y}, B_{0z}, x_0, y_0, z_0]. \quad (27)$$

As noted by P20, there is a degeneracy between \mathbf{B}_0 and c_0 such that c_0 cannot be constrained in the direction parallel to \mathbf{B}_0 .

Our goal is to infer a combination of parameters θ that yields a modeled \mathbf{B}_M consistent with the observed \mathbf{B} . We model the likelihood of the observed B-field at any given point on the Bubble’s surface \mathbf{B}_i given θ , $p(\mathbf{B}_i|\theta)$, with a Watson distribution,

$$\begin{aligned} p(\mathbf{B}_i|\theta) &= p(\pm\mathbf{B}_i | \mathbf{B}_M(\theta), \kappa_i) \\ &= \left(\frac{\sqrt{\pi} \operatorname{erfi}(\sqrt{\kappa_i})}{2\sqrt{\kappa_i}} \right)^{-1} \exp\left(\kappa_i (\mathbf{B}_M(\theta)^T \mathbf{B}_i)^2\right). \end{aligned} \quad (28)$$

We discuss the Watson distribution and the estimation of the concentration parameter κ in Appendix A. The log-likelihood of all \mathbf{B} given θ is the sum of the individual log-likelihoods, $\ln p(\mathbf{B}|\theta) = \sum_{i=1}^n \ln p(\mathbf{B}_i|\theta)$.

To evaluate the posterior distribution of the probability of θ given \mathbf{B} , $p(\theta|\mathbf{B}) = p(\mathbf{B}|\theta)p(\theta)/p(\mathbf{B})$, we perform dynamic nested sampling (Higson et al. 2019) as implemented in the python package *dynesty* (Speagle 2020). We use multiple bounding ellipsoids and uniform sampling. We adopt uniform priors on \mathbf{B}_0 and truncated normal priors on c_0 , requiring

$$\begin{aligned} \mathbf{B}_0 &\begin{cases} B_{x,0} \in [-1, 1] \\ B_{y,0} \in [0, 1] \\ B_{z,0} \in [-1, 1] \\ (B_{x,0}^2 + B_{y,0}^2 + B_{z,0}^2)^{1/2} = 1 \end{cases} \\ c_0 &\begin{cases} x_0 \sim \mathcal{N}(-10, 100) \in [-190, 190] \\ y_0 \sim \mathcal{N}(2, 118) \in [-280, 310] \\ z_0 \sim \mathcal{N}(0, 122) \in [-220, 350] \end{cases} \end{aligned} \quad (29)$$

We restrict $B_{y,0} \in [0, 1]$; relaxing this restriction causes our posteriors to converge on two equal but opposite-signed solutions ($(B_{x,0}, B_{y,0}, B_{z,0})$ and $(-B_{x,0}, -B_{y,0}, -B_{z,0})$), with no significant change to c_0 . We additionally place a joint prior on $(B_{x,0}, B_{y,0}, B_{z,0})$ so that \mathbf{B}_0 is a unit vector. Our priors on c_0 are centered on the geometric center of the O24 model of the Local Bubble, with widths determined by the standard deviation of the model’s coordinates. We truncate our volume at the $\pm 3\sigma$ quantiles of the O24 model’s $A_{0.5}$ “inner edge” of the Local Bubble’s shell to encode our assumption that c_0 falls in the interior of the present-day volume of the Local Bubble. We sample points from the Local Bubble’s surface at HEALPix $N_{\text{side}} = 32$ resolution for computational efficiency; we verify that estimates of θ do not change significantly with sampling resolution.

6.3.3. Modeling Results

Our posterior distribution of θ is centered on values of:

$$\begin{aligned} \hat{\mathbf{B}}_0 &\begin{cases} B_{x,0} = 0.504 \pm 0.003 \\ B_{y,0} = 0.863 \pm 0.002 \\ B_{z,0} = -0.027 \pm 0.003 \end{cases} \\ \hat{c}_0 &\begin{cases} x_0 = 15.0_{-104.9}^{+110.1} \text{ pc} \\ y_0 = -21.8_{-180.0}^{+188.1} \text{ pc} \\ z_0 = -3.9_{-6.0}^{+5.7} \text{ pc}, \end{cases} \end{aligned} \quad (30)$$

where reported uncertainties mark the 95% (2σ) credible intervals. We emphasize that the uncertainties on y_0 and x_0 are much larger than on z_0 due to the degeneracy between \mathbf{B}_0 and c_0 in the direction of \mathbf{B}_0 . A corner plot showing the posterior distribution of these variables is presented in Appendix C.

In Appendix B, we test the accuracy of our B-field orientation inference method using the M23 simulated bubble; we derive an angular distance between our inferred $\hat{\mathbf{B}}_0$ and the true initial B-field orientation in the simulated volume of 3.9° . This provides a zeroth-order constraint on the accuracy of the initial orientation inferred from the observed Local Bubble in this work.

In 2D Galactic coordinates, our derived $\hat{\mathbf{B}}_0$ is oriented towards $(\ell_0, b_0) = (59.70^\circ \pm 0.09^\circ, -1.55^\circ \pm 0.08^\circ)$. As discussed, Alves et al. (2018) and Pelgrims et al. (2020) previously inferred the 2D \mathbf{B}_0 from *Planck* 353 GHz observations at polar ($|b| \geq 60^\circ$) latitudes. Our inferred (ℓ_0, b_0) diverges from their inferred values. A18 adopted a scale-free elliptical model of the Local Bubble and derived an initial orientation towards $(\ell_0, b_0) = (71 \pm 11^\circ, -16 \pm 7^\circ)$. P20 used their 3D dust-derived model of the

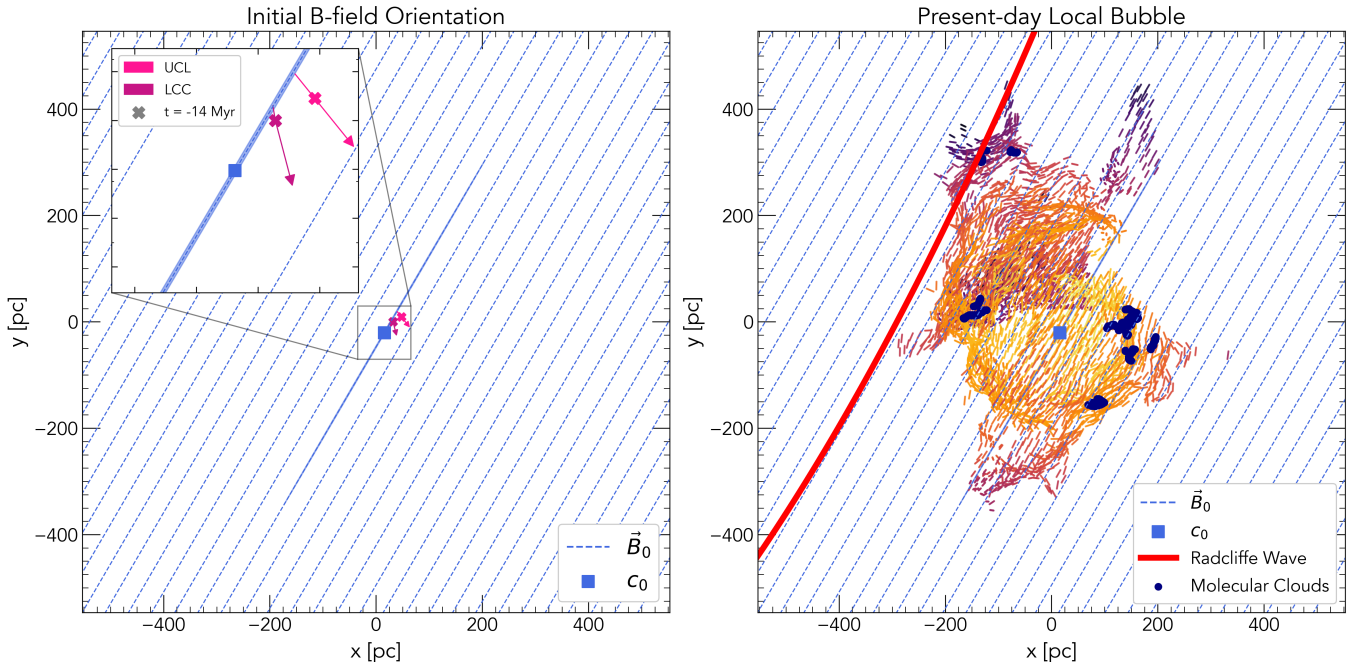


Figure 9. Best-fit values for the initial local Galactic Magnetic Field orientation, \mathbf{B}_0 , and the Local Bubble’s center of radial expansion, c_0 , are shown in the $x-y$ plane. *Left:* The orientation of \mathbf{B}_0 is shown by the dashed blue vectors extending across the solar neighborhood. The location of c_0 is marked by the blue square, with the 99.7% (3σ) credible interval on its location shown by the very thin blue ellipse oriented along \mathbf{B}_0 . The trajectories of the Upper Centaurus Lupus (UCL) and Lower Centaurus Lupus (LCC) stellar clusters derived by Zucker et al. (2022) are shown from cluster birth to $t = -10$ Myr by the light pink and dark pink arrows, respectively, with their positions at Zucker et al. (2022)’s estimated birth of the Local Bubble at $t = -14$ Myr marked by crosses. *Right:* As left, but additionally showing a model of the Radcliffe Wave in red (Konietzka et al. 2024), the locations of molecular clouds on the Local Bubble’s surface in navy (Zucker et al. 2021), and this work’s 3D model of the Local Bubble’s B-field (with vectors colored by distance from the Sun as in Figure 8).

Local Bubble to infer an initial orientation (for their $l_{\max} = 6$ model) towards $(\ell_0, b_0) = (73.2 \pm 0.1^\circ, 16.8 \pm 0.4^\circ)$ and an expansion center c_0 at $(x_0 = 57.6 \pm 34.5$ pc, $y_0 = 79.2 \pm 114.1$ pc, $z_0 = -86.3 \pm 36.1$ pc). P20 noted that their fit z_0 are located significantly below the Galactic plane, which is difficult to reconcile with the expectation of the Local Bubble’s progenitor supernovae population being centered in the disk. We experiment with fitting \mathbf{B}_0 and c_0 based only on the O24 model’s polar caps, and derive results in closer agreement to A18 and P20: $(\ell_0, b_0) = (67.93 \pm 0.46^\circ, 23.57^{+1.35}_{-1.43}^\circ)$ and an extraplanar $z_0 = -57.7^{+91.2}_{-88.9}$ pc. We attribute this result to the lack of geometrical constraints provided by in-disk portions of the Local Bubble’s shell, and/or to a potential shift in mean B-field orientation in the present day in the polar caps vs. over the full surface of the Local Bubble.

7. DISCUSSION

Our present-day model of the Local Bubble’s B-field is on average oriented towards $\bar{\ell}_B \sim 60 - 70^\circ$ and $\bar{b}_B \sim 0^\circ$, depending on the region of the sky considered. These values are generally consistent with previous estimates

of large-scale interstellar B-field orientations in the Solar Neighborhood. Planck Collaboration et al. (2016a) modeled the structure of the GMF over the Southern polar cap and derived a mean orientation towards $(\ell_B, b_B) = (70^\circ, 24^\circ)$, which is similar, though not identical, to what we have derived for the Southern cap of the Local Bubble. Studies of starlight polarization near the Local Bubble have derived orientations towards $(\ell_B, b_B) = (80^\circ, 0^\circ)$ (Heiles 1996), while analysis of pulsar rotation measures has yielded $\ell_B = 77^\circ$ (Rand & Kulkarni 1989, when including LOS that intersect the North Polar Spur).

Understanding what portion of these measurements arises from the Local Bubble’s B-field vs. the more distant, large-scale Galactic B-field requires detailed, 3D studies of polarization as a function of distance and on-sky position. Through analysis of starlight polarization within 500 pc, Gontcharov & Mosenkov (2019) observed a steep jump in starlight polarization degree at a distance of ~ 100 pc, which they associated with the transition from the interior to the exterior of the Local Bubble. Skalidis & Pelgrims (2019) found evidence for the Local Bubble affecting starlight polarization fraction and ori-

entation through analysis of starlight polarization relative to *Planck* 353 GHz data, while [Medan & Andersson \(2019\)](#) analyzed starlight polarization data and demonstrated that the strength of the Local Bubble’s magnetic field and the efficiency of grain alignment likely varies significantly across its surface.

Our analysis of dust and starlight polarization metrics in this work demonstrates that passage through the Local Bubble’s shell likely has a significant effect on observed polarization over much of the sky, in agreement with previous studies but benefiting from the additional 3D information contributed by the O24 Local Bubble model. Notably, we find the most consistent and dramatic changes in starlight polarization fraction and orientation relative to *Planck* occur in the region of the Northern sky above the Galactic center containing the well-known Loop I polarization feature. Through comparison of starlight polarization as a function of distance relative to synchrotron emission, [Panopoulou et al. \(2021\)](#) derived distance estimates to the Loop I feature ranging between $d < 105$ pc to $d = 135 \pm 20$ pc. These distance estimates are consistent with the distances to the O24 Local Bubble shell (91–147 pc) along the same LOS analyzed by [Panopoulou et al. \(2021\)](#), suggesting that the Loop I polarization orientation originates in the Local Bubble’s shell.

On the whole, our analysis provides support for the idea that a significant fraction of polarization features originate near the Sun at the Local Bubble’s magnetized shell. In addition, we observe a transition from random to ordered starlight polarization orientation as one moves from the interior of the Local Bubble to its shell. This suggests that at least three components are needed to properly model B-fields observed by *Planck* and similar facilities: 1) the weakly magnetized interior of the Local Bubble, where polarization orientation is nearly random, 2) the coherent, magnetized shell of the Local Bubble, and 3) the large-scale Galactic magnetic field.

Finally, we consider what the inferred orientation of the initial Galactic magnetic field (\mathbf{B}_0) in the solar neighborhood can reveal about the evolution of the Local Bubble. [Figure 9](#) shows the orientation of our best-fit \mathbf{B}_0 in the context of the present-day solar neighborhood. Theory and simulations predict that superbubbles preferentially expand parallel to their environment’s initial B-field, and are hindered in expanding in the perpendicular direction (e.g., [Tomisaka 1998](#); [Ntormousi et al. 2017](#)). We infer a \mathbf{B}_0 that is mostly oriented in the y -direction, with a moderate x component and a negligible vertical z component. The O24 Local Bubble model is more extended in the y and z directions compared

to the x direction (with aspect ratios of $\delta y/\delta x = 1.3$, $\delta z/\delta x = 1.4$). Additionally, most of the star-forming molecular clouds on the Local Bubble’s surface (Taurus, Chamaeleon, Corona Australis, Musca, Lupus, Ophiuchus, Pipe, & Cepheus), whose formation [Zucker et al. \(2022\)](#) showed was likely triggered by the expansion of the Local Bubble, are situated along the axis perpendicular to \mathbf{B}_0 .

The elongation of the Local Bubble in the direction parallel to \mathbf{B}_0 , and its relative compression (and resulting star formation) in the perpendicular direction, is consistent with theoretical predictions for bubble expansion in the magnetized ISM. We expect that the vertical elongation of the Local Bubble into a northern “Chimney” feature is more likely to be the result of vertically-stratified ISM gas density, dynamics, and past star formation activity than of initial B-field strength or orientation; see [O’Neill et al. \(2024\)](#) for further discussion.

We additionally consider the relevance of our derived center of radial expansion, c_0 , in the context of expectations for the feedback-driven evolution of the Local Bubble. Our best-fit c_0 is unconstrained in the direction of \mathbf{B}_0 , tracing out a thin region of plausible c_0 throughout the interior of the Local Bubble. By calculating stellar tracebacks, [Zucker et al. \(2022\)](#) suggested that the Upper Centaurus Lupus (UCL) and Lower Centaurus Crux (LCC) clusters in the Sco-Cen association may have hosted the progenitor supernovae that drove the Local Bubble’s expansion $t = -14$ Myr ago. We show their derived trajectories of UCL and LCC from cluster birth (at $t = -16$ Myr and $t = -15$ Myr, respectively) until $t = -10$ Myr in [Figure 9](#). We find that the UCL and LCC clusters both intersect the range of possible c_0 in the $x - y$ plane at their estimated birth times (although they are negatively offset in the z direction by about 15–20 pc). This general agreement suggests that UCL and LCC are indeed plausible candidates for launching the radial expansion of the Local Bubble, as has long been proposed in the literature (see [Fuchs et al. 2006](#); [Maíz-Apellániz 2001](#)).

Finally, we explore the alignment between the Local Bubble’s B-field and the local segment of the Radcliffe Wave, a kiloparsecs-long collection of molecular clouds that is likely the gaseous component of the local arm of the galaxy ([Alves et al. 2020](#); [Swiggum et al. 2022](#); [Konietzka et al. 2024](#)). We observe that the local portion of the Radcliffe Wave is oriented parallel to \mathbf{B}_0 in the x - y plane. This alignment is consistent with the theoretical expectation and extragalactic observational evidence that galactic-scale magnetic fields tend to align

with spiral structure (see e.g., Beck & Wielebinski 2013, for a review).

In total, our analysis suggests that the nascent Local Bubble encountered a magnetic field aligned with the Galactic spiral structure, and that the Local Bubble’s subsequent expansion and resultant molecular cloud and star formation proceeded to preferentially occur along axes determined by the local magnetic field.

8. CONCLUSIONS

In this work, we derive a 3D model of magnetic field orientation on the surface of the Local Bubble by combining *Planck* dust polarization observations, optical starlight polarimetry, and assumptions about the behavior of magnetic fields on the surface of superbubbles. Our main conclusions are as follows:

1. We introduce a novel method to reconstruct 3D B-field orientation from 2D polarization orientation (§3) and apply it to the Local Bubble. Application of this method to a simulated superbubble also indicates it provides a reasonable representation of the true 3D B-field structure (§5, Appendix B).
2. Significant correlations exist between properties of the Local Bubble’s shell (such as density and inclination to the plane-of-the-sky) and metrics of both dust and starlight polarization (§4). Over most lines-of-sight, starlight polarization fraction increases and starlight polarization orientation transitions towards alignment with *Planck* polarization orientation at the Local Bubble’s shell.
3. We model the initial orientation of the Galactic Magnetic Field in the solar neighborhood (§6), and find an orientation parallel to the gaseous component of the local arm of the galaxy (the Radcliffe Wave). We find that the Local Bubble is more extended in the direction parallel to our inferred initial orientation, and that molecular clouds on the Local Bubble’s shell are preferentially concentrated in the perpendicular direction.

Overall, this work suggests that the Local Bubble’s magnetized shell significantly influences our view of Galactic polarization, and that the Local Bubble’s evolution has been shaped by interstellar magnetic fields. Future efforts to reconstruct the 3D B-field on the Local Bubble’s surface — independent of our Assumption I and Assumption II— could combine starlight polarization tomography (e.g., Panopoulou et al. 2019b; Pelgrims et al. 2023, 2024) with line-of-sight B-field probes such as Faraday rotation measures (e.g., Ferrière 2016;

Tahani et al. 2018, 2022b). Upcoming extensive polarization surveys such as PASIPHAE (Tassis et al. 2018) will play a crucial role in the construction of higher resolution, tomographic decompositions of the Local Bubble’s magnetic field.

Finally, corrections for Galactic polarization in studies of the Cosmic Infrared/Microwave Backgrounds and modeling of the Galactic scale magnetic fields should account for local foreground contributions by the Local Bubble. Identifying the structure of the Local Bubble’s magnetized shell offers a path toward correcting the foreground contribution to these observations and Galactic-scale models. Furthermore, it will reveal in detail the interplay between magnetization and stellar feedback in the nearest laboratory of ISM physics.

We thank Efrem Maconi, Susan Clark, George Halal, Ralf Klessen, Gina Panopoulou, João Alves, and Micah Acinapura for insightful discussions. T.J.O. acknowledges that this material is based upon work supported by the National Science Foundation Graduate Research Fellowship under Grant No. DGE 2140743. T.J.O., A.A.G., and C.Z. acknowledge support by NASA ADAP grant 80NSSC21K0634 “Knitting Together the Milky Way: An Integrated Model of the Galaxy’s Stars, Gas, and Dust.” T.J.O. and A.A.G. acknowledge support from National Science Foundation grants 2209623 and 1908419. The SAO REU program is funded in part by the National Science Foundation REU and Department of Defense ASSURE programs under NSF Grant no. AST-2050813, and by the Smithsonian Institution (T.J.O.). J.D.S is funded by the European Research Council via the ERC Synergy Grant “ECOGAL – Understanding our Galactic ecosystem: From the disk of the Milky Way to the formation sites of stars and planets” (Project ID 855130). The authors acknowledge Interstellar Institute’s program “With Two Eyes” and the Paris-Saclay University’s Institut Pascal for hosting discussions that nourished the development of the ideas behind this work.

Interactive Figures: Interactive figures presented in this work can be accessed at: <https://theo-oneill.github.io/magneticlocalbubble/>.

Data Access: The derived models of the Local Bubble’s 3D Magnetic Field can be downloaded from the Harvard Dataverse: <https://doi.org/10.7910/DVN/A8HWUF>, including:

- Table of Local Bubble’s 3D B-field orientation
- Standalone HTML files of interactive figures

Software: Astropy (Astropy Collaboration et al. 2013, 2018, 2022); Cmasher (van der Velden 2020); connected-components-3d (Silversmith 2021); Dustmaps (Green 2018); dynesty (Speagle 2020); glue

(Robitaille et al. 2019); Healpy (Zonca et al. 2019); K3d-jupyter (Trzesiok et al. 2021); Matplotlib (Hunter 2007); Numpy (Harris et al. 2020); OpenSpace (Bock et al. 2017); Pandas (McKinney 2010); PyVista (Sullivan & Kaszynski 2019)

APPENDIX

A. UNCERTAINTY ESTIMATION ON 3D B-FIELD

Our derived 3D magnetic field model \mathbf{B} is a field of axially symmetric unit vectors, i.e., vectors defined by orientation but not direction ($\mathbf{B} = -\mathbf{B}$), with associated uncertainties. A natural model for this field is the Watson distribution (Watson 1965; Mardia & Jupp 2000), which describes axially symmetric p -dimensional vectors on the S^{p-1} unit hypersphere. The Watson distribution's probability distribution function for $p = 3$ -dimensional vectors is given by,

$$p(\pm\mathbf{B}|\boldsymbol{\mu}_B, \kappa_B) = \mathcal{M}\left(\frac{1}{2}, \frac{3}{2}, \kappa_B\right)^{-1} \exp(\kappa_B(\boldsymbol{\mu}_B^T \mathbf{B})^2), \quad (\text{A1})$$

where $\mathbf{B} = (B_x, B_y, B_z)^T$, $\boldsymbol{\mu}_B = (\mu_{B,x}, \mu_{B,y}, \mu_{B,z})^T$ is the mean orientation, and $\mathcal{M}\left(\frac{1}{2}, \frac{p}{2}, \kappa\right)$ is the Kummer function,

$$\mathcal{M}\left(\frac{1}{2}, \frac{3}{2}, \kappa_B\right) = \frac{\sqrt{\pi} \operatorname{erfi}(\sqrt{\kappa_B})}{2\sqrt{\kappa_B}}. \quad (\text{A2})$$

κ_B is a parameter describing the concentration of the probability distribution function around $\pm\boldsymbol{\mu}_B$; larger positive values of κ_B correspond to greater concentration. Note that this distribution enforces rotational symmetry around the axis defined by $\pm\boldsymbol{\mu}_B$.

To quantify our uncertainties on $\mathbf{B} = \mathbf{B}(\psi_\perp, \mathbf{n})$, we must estimate the parameters of the Watson distribution $\mathcal{W}(\boldsymbol{\mu}_B, \kappa_B)$ describing each B-field vector. We estimate these parameters via a Monte Carlo approach, where we incorporate two main sources of uncertainty: uncertainties contributed by the *Planck* dust polarization angles ψ_\perp , and uncertainties contributed by the orientation of the Local Bubble's shell in 3D space as defined by the normal vector \mathbf{n} .

A.1. *Planck*-based Uncertainties

To estimate *Planck*-derived uncertainties, we first generate versions of the *Planck* GNILC I , Q , and U covariance maps smoothed to our adopted 2° resolution. Following Planck Collaboration et al. (2020c), we consider these observed parameters as originating from a multivariate Gaussian distribution centered at the *Planck* measurements $\boldsymbol{\mu}_{planck} = (I, Q, U)^T$ with covariances defined as \mathbb{C}_{planck} . Since ψ_\perp is defined by Q and U , we

can then generate random realizations of ψ_\perp by sampling from $(I, Q, U) \sim \mathcal{N}(\boldsymbol{\mu}_{planck}, \mathbb{C}_{planck})$.

A.2. *Inclination-based Uncertainties*

To estimate inclination-derived uncertainties, we make use of the $n_{draw} = 12$ draws of the Edenhofer et al. (2024) dust map, which O24 used to characterize uncertainty in their model of the Local Bubble. As part of this analysis, O24 derived a model of the Local Bubble from each draw and fit all associated properties including \mathbf{n} . Since \mathbf{n} is a directed unit vector, we can consider its distribution as being characterized by a 3D von Mises-Fisher (vMF) distribution (von Mises 1918; Fisher 1953; Mardia & Jupp 2000), which describes directed p -dimensional vectors on the S^{p-1} unit hypersphere. The vMF distribution's probability distribution function for $p = 3$ is given by,

$$p(\mathbf{n}|\boldsymbol{\mu}_n, \kappa_n) = \left(\frac{\kappa_n}{4\pi \sinh \kappa_n}\right) \exp(\kappa_n(\boldsymbol{\mu}_n^T \mathbf{n})), \quad (\text{A3})$$

where $\mathbf{n} = (n_x, n_y, n_z)^T$, $\boldsymbol{\mu}_n = (\mu_{n,x}, \mu_{n,y}, \mu_{n,z})^T$ is the mean direction, and κ_n is the concentration parameter (with similar interpretation to κ in the Watson distribution). The mean direction $\boldsymbol{\mu}_n$ can be estimated as

$$\hat{\boldsymbol{\mu}}_n = \frac{1}{\bar{r}} \left[\frac{1}{n_{draw}} \sum_{j=1}^{n_{draw}} \mathbf{n}_{draw,j} \right], \quad (\text{A4})$$

where $\bar{r} = \frac{1}{n_{draw}} \|\sum_j \mathbf{n}_{draw,j}\|$ is the mean resultant length. Concentration κ_n can be estimated from \bar{r} using the approximation derived by Banerjee et al. (2005),

$$\hat{\kappa}_n \simeq \frac{\bar{r}(3 - \bar{r}^2)}{1 - \bar{r}^2}. \quad (\text{A5})$$

We are then free to generate random realizations of \mathbf{n} as $\mathbf{n} \sim \mathcal{VMF}(\hat{\boldsymbol{\mu}}_n, \hat{\kappa}_n)$.

A.3. *Combined Uncertainties*

For each point on the Local Bubble's surface, we produce $n_{samp} = 10,000$ random samples from $\mathcal{N}(\boldsymbol{\mu}_{planck}, \mathbb{C}_{planck})$ and $\mathcal{VMF}(\hat{\boldsymbol{\mu}}_n, \hat{\kappa}_n)$. We project the resulting n_{samp} pairs of ψ_\perp and \mathbf{n} to n_{samp} 3D B-field vectors \mathbf{B}_{samp} using the procedure outlined in

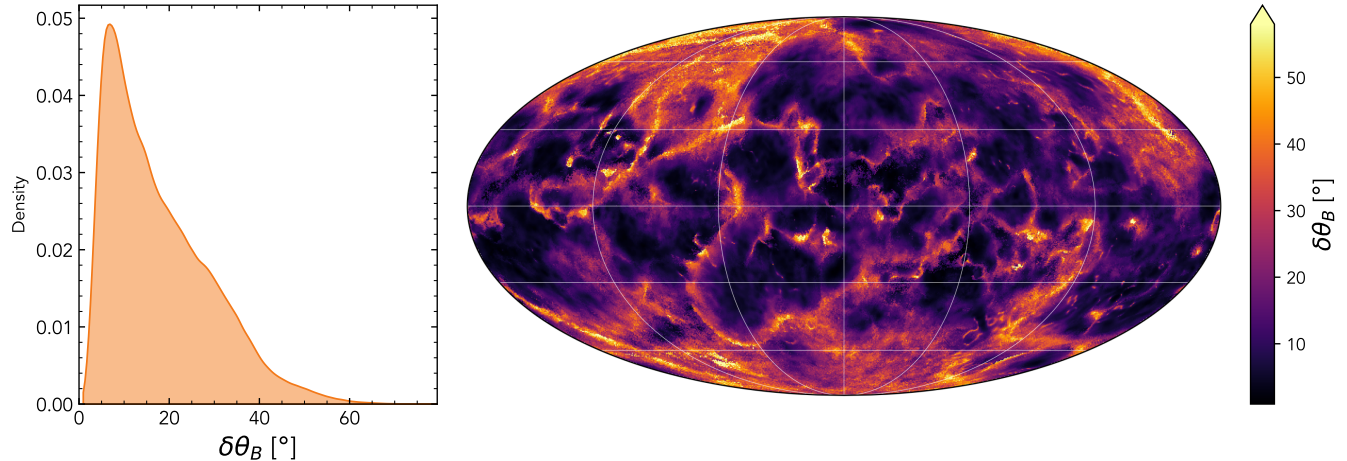


Figure A1. *Left:* Kernel density estimation of average uncertainty on 3D vector orientation, $\delta\theta_B$, derived from our Monte Carlo experiments. *Right:* Mollweide projection of $\delta\theta_B$.

§3.2. We can now proceed to use $\mathbf{B}_{s\text{amp}}$ to characterize $\mathcal{W}(\boldsymbol{\mu}_B, \kappa_B)$.

The mean direction $\boldsymbol{\mu}_B$ can be estimated as the first eigenvector of the scatter matrix, (Mardia & Jupp 2000),

$$\mathbf{S} = \frac{1}{n_{s\text{amp}}} \sum_{j=1}^{n_{s\text{amp}}} \mathbf{B}_{s\text{amp},j} \mathbf{B}_{s\text{amp},j}^T, \quad (\text{A6})$$

$$\hat{\boldsymbol{\mu}}_B = \mathbf{s}_1 \text{ if } \hat{\kappa}_B > 0. \quad (\text{A7})$$

To find the maximum likelihood estimate of κ_B , we must find the solution to the relationship,

$$\hat{\boldsymbol{\mu}}_B^T \mathbf{S} \hat{\boldsymbol{\mu}}_B = \frac{\mathcal{M}'\left(\frac{1}{2}, \frac{3}{2}, \hat{\kappa}_B\right)}{\mathcal{M}\left(\frac{1}{2}, \frac{3}{2}, \hat{\kappa}_B\right)}. \quad (\text{A8})$$

We solve for $\hat{\kappa}_B$ numerically, as no closed-form solution to Eqn. A8 exists. We impose a maximum $\hat{\kappa}_B = 600$ to prevent overflow in the evaluation of the Watson PDF for very concentrated distributions; 0.2% of vectors in \mathbf{B} require this upper limit. Derived values of $\hat{\kappa}_B$ range between 0.40 and 600, with a mean of 32.6.

We additionally summarize the uncertainty on B-field orientation at each point on the Local Bubble's surface by computing the mean angular difference between \mathbf{B}_i and $\mathbf{B}_{s\text{amp}}$,

$$\delta\theta_{B_i} = \frac{1}{n_{s\text{amp}}} \sum_{j=1}^{n_{s\text{amp}}} \cos^{-1}(|\mathbf{B}_i \cdot \mathbf{B}_{s\text{amp},j}|). \quad (\text{A9})$$

We provide a histogram and 2D projected view of $\delta\theta_B$ in Figure A1. $\delta\theta_B$ ranges between 0.94° and 79.4° , with a mean of 17.8° . θ_B is strongly negatively correlated with Local Bubble shell density n_{peak} ($\rho_s = -0.72$, $p < 0.001$), i.e., uncertainties on 3D B-field orientation tend

to be lower in high-density regions of the shell, where variation between draws of the Edenhofer et al. (2024) dust map is low.

B. PERFORMANCE FOR A SIMULATED LOCAL BUBBLE EQUIVALENT

To test the accuracy of our B-field projection method and the assumptions guiding this work, we apply our method to a simulated analog of the Local Bubble analyzed by Maconi et al. (2023, hereafter M23). M23 analyzed snapshots from the Girichidis et al. (2018) and Girichidis (2021) simulations (created as part of the SILCC project, Walch et al. 2015; Girichidis et al. 2016) of supernova-driven superbubbles evolving in a magnetized $(500 \text{ pc})^3$ volume of the ISM and identified a superbubble with similar physical properties to the real Local Bubble (including B-field strength and shell density). Similar to the real Local Bubble, the M23 simulated bubble has also formed an asymmetric Chimney out of the disk.

M23 then generated synthetic 353 GHz polarization maps (Stokes I , Q , and U) for an observer in the center of the bubble using the POLARIS radiative transfer code (Reissl et al. 2016). In this appendix, we combine these simulated 2D polarization maps with the ground-truth 3D B-field orientation within the shell of the simulated bubble to test the accuracy of our 3D B-field projection method, and our assumption of 3D B-field tangency to the superbubble's shell. M. Kunold et al. (in preparation) will analyze the performance of the assumption of B-field tangency for the simulated bubble in greater depth.

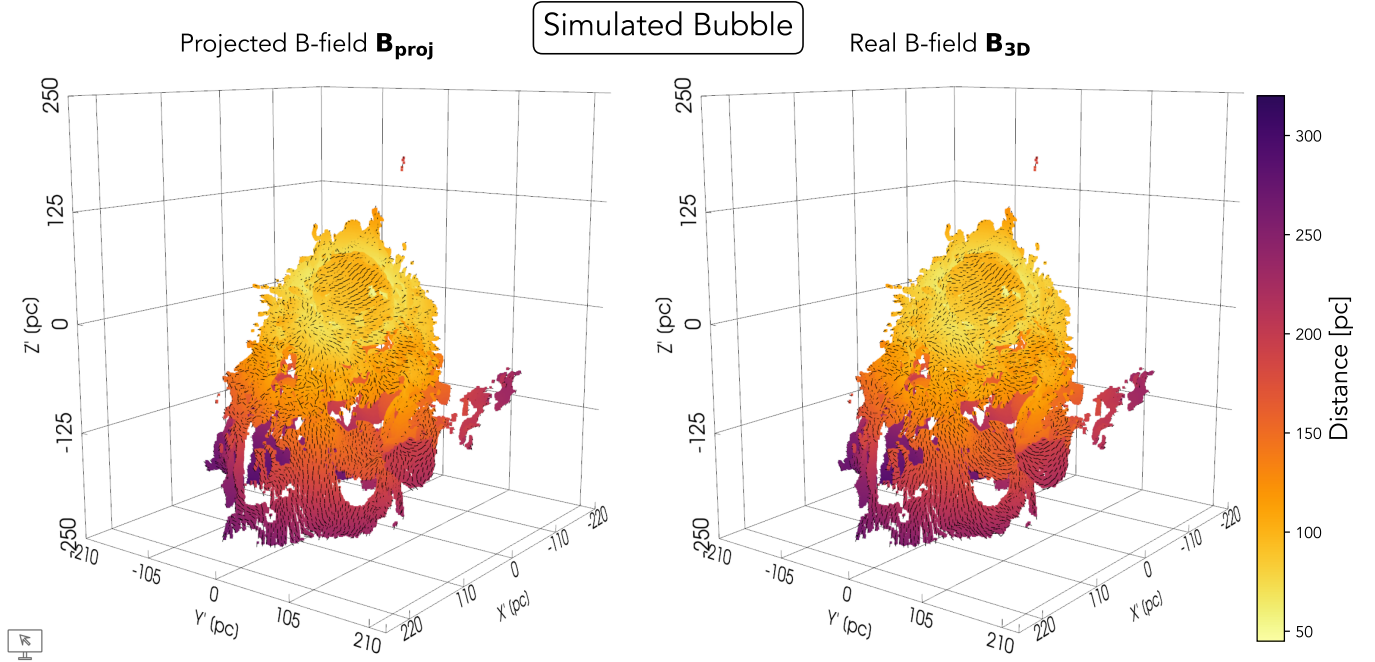


Figure B1. *Left:* 3D B-field model derived via our fiducial projection method, \mathbf{B}_{proj} , for a simulated equivalent of the Local Bubble. \mathbf{B}_{proj} is shown by the black vectors, overlaid on a model of the simulated bubble’s shell colored by distance from the observer. *Right:* As left, but showing the real 3D B-field on the surface of the simulated bubble, \mathbf{B}_{3D} . Interactive figure is available online at: https://theo-oneill.github.io/magneticlocalbubble/sim_Bfield/

B.1. Modeling the Simulated Bubble

To assess our method’s performance, we first generate a model of the simulated bubble’s peak density surface using the same peak-finding method employed by O’Neill et al. (2024) to model the Local Bubble’s shell. This method identifies the first prominent peak along the LOS from an observer at the center of the bubble being mapped. Although this basic principle holds regardless of use case, a key difference between the application of this method to real vs. simulated bubbles is that simulated volumes (like the simulated 3D gas density map analyzed by M23) are able to reveal structures of all densities in and around bubbles, while current 3D dust mapping techniques are only sensitive to a limited range of densities. Inspection of the M23 gas density map reveals a variety of extremely diffuse filaments and sheets in the interior of the simulated bubble that are not a part of the bubble’s shell and would not be resolved by 3D dust maps, but would interfere with our peak-finding procedure.

To map the simulated bubble’s shell using the O24 method while overlooking these ultra-low-density structures, we perform a multi-step cleaning procedure which we emphasize was developed on an ad-hoc basis for the specific conditions of this simulation. Specific parameters described below were selected via experimentation

with an eye towards reducing contamination of the final bubble shell model by interior structures. Working in cartesian space, we first identify and mask all material in the gas cube below a density of $n = 10^{-1} \text{ cm}^{-3}$. This removes the majority of low-density contaminants but leaves behind several isolated intermediate-density cores in the bubble’s interior. We identify these isolated cores in our thresholded map using the python package `connected-components-3D` (Silversmith 2021) and mask them out as well. We additionally mask pixels with low B-field strengths ($|B| < 1\mu\text{G}$). For gas more than 3 scale-heights ($H = 30 \text{ pc}$, Girichidis et al. 2018) above and below the simulated bubble’s center, we perform a similar procedure with a gas density threshold of $n = 10^{-2} \text{ cm}^{-3}$ and no B-field strength requirement. In total, this cleaning process yields a cartesian gas density map analogous to what might be resolved by current 3D dust mapping techniques and suitable for application of the O24 peak-finding method.

We project this cleaned gas density map to a spherical coordinate system defined at HEALPix $N_{\text{side}} = 256$ sampling with 1 pixel (0.98 pc) radial spacing. We apply the O24 peak-finding method to this spherical volume, smoothing each LOS with a Gaussian kernel of $\sigma = 3$ pixel (2.94 pc) and requiring a minimum prominence of 10^{-2} cm^{-3} . This yields a 3D map of the simulated

bubble with the same set of properties derived by O24 in their model of the Local Bubble, including shell distance, density, and inclination. We then apply the B-field projection procedure described in §3.2 to the simulated bubble. We first match the M23 simulated 2D Stokes I , Q , and U polarization maps to each LOS in the simulated Bubble's shell, and then project the corresponding B-field angles to 3D to infer the B-field orientation \mathbf{B}_{proj} . The resulting 3D models of the bubble and \mathbf{B}_{proj} are shown in Figure B1.

B.2. Accuracy of Projection Method

Our B-field projection model relies on the assumptions that: I) polarization orientation originates at the bubble's magnetized shell, and II) the bubble's B-field is tangent to the bubble shell. We can directly test the validity of these assumptions for the M23 simulated bubble by comparing our projected B-field orientation \mathbf{B}_{proj} to the true orientation of the B-field at each point on the shell's surface \mathbf{B}_{3D} . \mathbf{B}_{proj} and \mathbf{B}_{3D} are both shown in Figure B1.

We first quantify the validity of our tangency assumption (Assumption II) by calculating the difference in orientation between \mathbf{B}_{3D} and the tangent plane fit to the simulated bubble's surface (characterized by the normal vector \mathbf{n}). We define a metric

$$\delta\theta_{tang} = 90^\circ - \cos^{-1}(|\mathbf{B}_{3D} \cdot \mathbf{n}|), \quad (\text{B1})$$

where $\delta\theta_{tang} = 0^\circ$ indicates parallel alignment and $\delta\theta_{tang} = 90^\circ$ indicates perpendicular alignment. Figure B2 shows a histogram of $\delta\theta_{tang}$ compared to the same statistic derived for two random 3D B-fields. $\delta\theta_{tang}$ has a median value of 13° . As assessed by a one-sided Kolmogorov-Smirnov test, the distribution of $\delta\theta_{tang}$ takes on values significantly closer to parallel alignment than for a random field ($p < 0.001$).

We then quantify the combined validity of Assumption I and Assumption II by calculating the agreement between \mathbf{B}_{3D} and \mathbf{B}_{proj} , defining a similar metric

$$\delta\theta_{proj} = \cos^{-1}(|\mathbf{B}_{3D} \cdot \mathbf{B}_{proj}|), \quad (\text{B2})$$

where $\delta\theta_{proj} = 0^\circ$ again indicates parallel alignment. Figure B2 also shows a histogram of $\delta\theta_{proj}$ compared to the same statistic derived for two random 3D B-fields. $\delta\theta_{proj}$ has a median value of 33° . As with our assumption of tangency, $\delta\theta_{proj}$ significantly outperforms a random field ($p < 0.001$). We observe that $\delta\theta_{proj}$ generally performs worse than $\delta\theta_{tang}$ alone, which is unsurprising given the additional strong assumption introduced.

Several weak-to-moderate correlations exist between $\delta\theta_{tang}$, $\delta\theta_{proj}$, and properties of the simulated bubble's

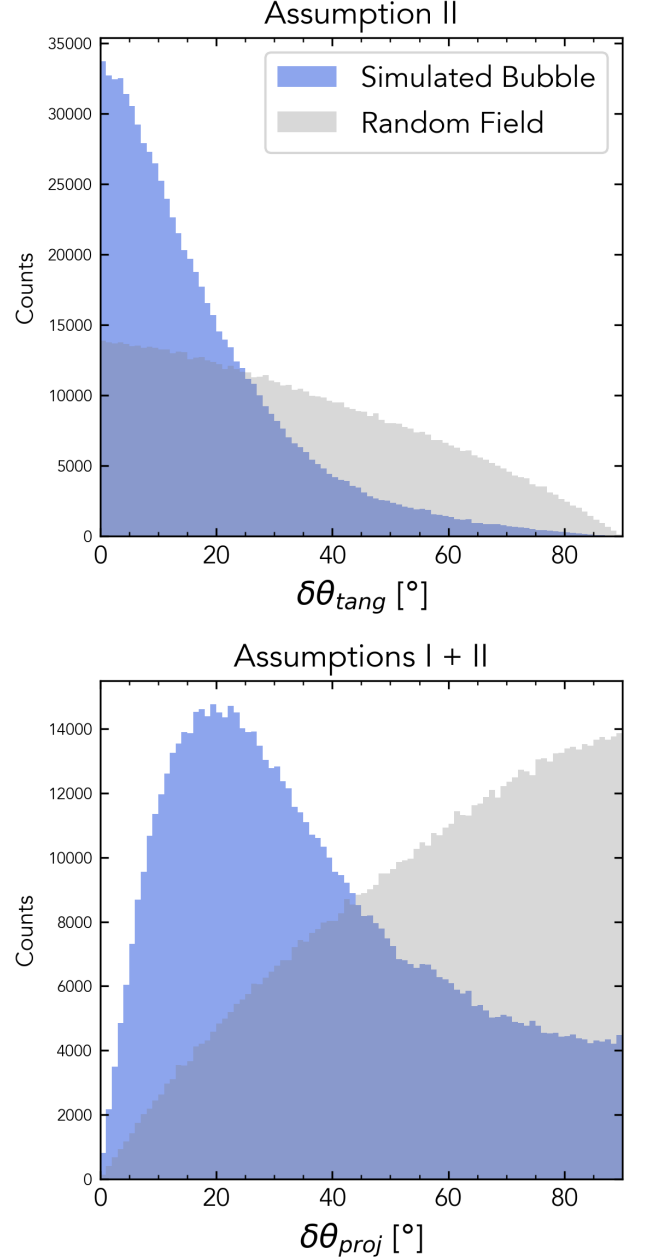


Figure B2. *Top:* Histogram of the performance of our Assumption II for the simulated bubble, as traced by our defined metric $\delta\theta_{tang}$, is shown in blue. The performance of this metric for a randomly oriented field is shown in gray. *Bottom:* As top, but for the performance of our combined Assumption I and Assumption II as traced by a metric $\delta\theta_{proj}$.

shell (n_{peak} , $|B|$, R_{SB} , γ), as summarized in Figure B3. A weak negative trend holds between $\delta\theta_{proj}$ and shell B-field strength $|B|$ ($\rho_s = -0.25$), indicating slightly improved performance of our combined Assumption I and Assumption II with increasing B-field strength. A weak positive trend holds between $\delta\theta_{proj}$ and shell inclination

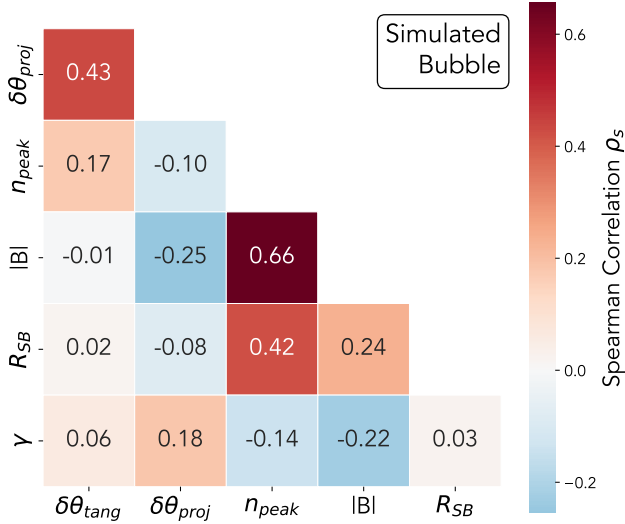


Figure B3. Matrix of Spearman correlation coefficients between $\delta\theta_{tang}$, $\delta\theta_{proj}$, and properties of the simulated bubble's shell (n_{peak} , $|B|$, R_{SB} , and γ).

γ , suggesting that the ability of the magnetized shell to contribute to polarization orientation decreases with increasing γ . A weak positive trend holds between $\delta\theta_{tang}$ and n_{peak} , suggesting that the superbubble's B-field is less likely to be tangent to the shell as gas density increases. We emphasize the overall weak nature of these correlations.

B.3. Correlations between Bubble Properties and 353 GHz Polarization Metrics

In §4.1, we analyzed various correlations between properties of the observed Local Bubble and *Planck* polarization metrics. In this section, we reproduce this analysis for the simulated bubble. As in §4.1, we restrict our analysis to LOS where the simulated bubble contributes more than 20% of the total integrated gas density along the LOS ($R_{SB} \geq 0.2$, slightly less than the median $R_{SB} = 0.23$).

The top row of Figure B4 displays correlations between peak shell density n_{peak} and the simulated Stokes I , P and p maps; the bottom row displays correlations between shell inclination γ and I/n_{peak} , P/n_{peak} , and p . Nearly all correlations take on similar trends and strengths to those observed for the real Local Bubble and *Planck* data. The exception is p vs. n_{peak} , which displays a weak positive correlation that is not present in the observed *Planck*–Local Bubble correlation analysis. In the subset of simulated LOS where the true 3D B-field's orientation is closest to tangency to the simulated bubble's shell (defined here as being within 5° of

perfect tangency), the lack of correlation between p and the γ -derived term persists ($\rho_s = 0.04$).

B.4. Accuracy of Initial B-field Orientation Modeling

Finally, we test the accuracy of our ability to reconstruct the initial orientation of the B-field in the ISM surrounding a present-day superbubble, like we do in §6 for the Local Bubble. The simulated volume containing the M23 superbubble was initialized with a uniform magnetic field oriented in the direction $\mathbf{B}_0 = (B_{x',0}, B_{y',0}, B_{z',0}) = (1, 0, 0)$.⁵

We perform our modeling procedure for the simulated \mathbf{B}_{proj} largely as described in §6, with the only change coming in our priors, which are selected to be appropriate for the center and $A_{0.9}$ extent of the simulated bubble:

$$\mathbf{B}_0 \begin{cases} B_{x',0} \in [0, 1] \\ B_{y',0} \in [-1, 1] \\ B_{z',0} \in [-1, 1] \\ (B_{x',0}^2 + B_{y',0}^2 + B_{z',0}^2)^{1/2} = 1 \end{cases} \quad (\text{B4})$$

$$c_0 \begin{cases} x'_0 \sim \mathcal{N}(-3, 62) \in [-140, 110] \\ y'_0 \sim \mathcal{N}(-1, 62) \in [-180, 130] \\ z'_0 \sim \mathcal{N}(-13, 69) \in [-230, 90]. \end{cases}$$

We define $\kappa_B = 1$ for all simulated LOS.

The corner plot for our inferred posterior is shown in Figure B5. Our posterior distribution is centered on values of:

$$\hat{\mathbf{B}}_0 \begin{cases} B_{x',0} = 0.998 \pm 0.001 \\ B_{y',0} = 0.021^{+0.015}_{-0.017} \\ B_{z',0} = 0.064^{+0.012}_{-0.011} \end{cases} \quad (\text{B5})$$

$$\hat{c}_0 \begin{cases} x'_0 = -6.9^{+102.0}_{-106.3} \text{ pc} \\ y'_0 = -3.0^{+2.3}_{-3.2} \text{ pc} \\ z'_0 = -1.4^{+6.8}_{-7.0} \text{ pc}, \end{cases}$$

⁵ M23 defined a Cartesian coordinate system that we refer to as (x', y', z') where the $-y'$ direction points towards $(\ell, b) = (0^\circ, 0^\circ)$. This relates to the Cartesian coordinate system that we use in the bulk of this work (where the $+x$ direction points towards $(\ell, b) = (0^\circ, 0^\circ)$) as,

$$\begin{aligned} x' &= -d \sin(\ell) \cos(b) = -y \\ y' &= -d \cos(\ell) \cos(b) = -x \\ z' &= d \sin(b) = z. \end{aligned} \quad (\text{B3})$$

While analyzing the M23 bubble, we make use of the M23 coordinate system.

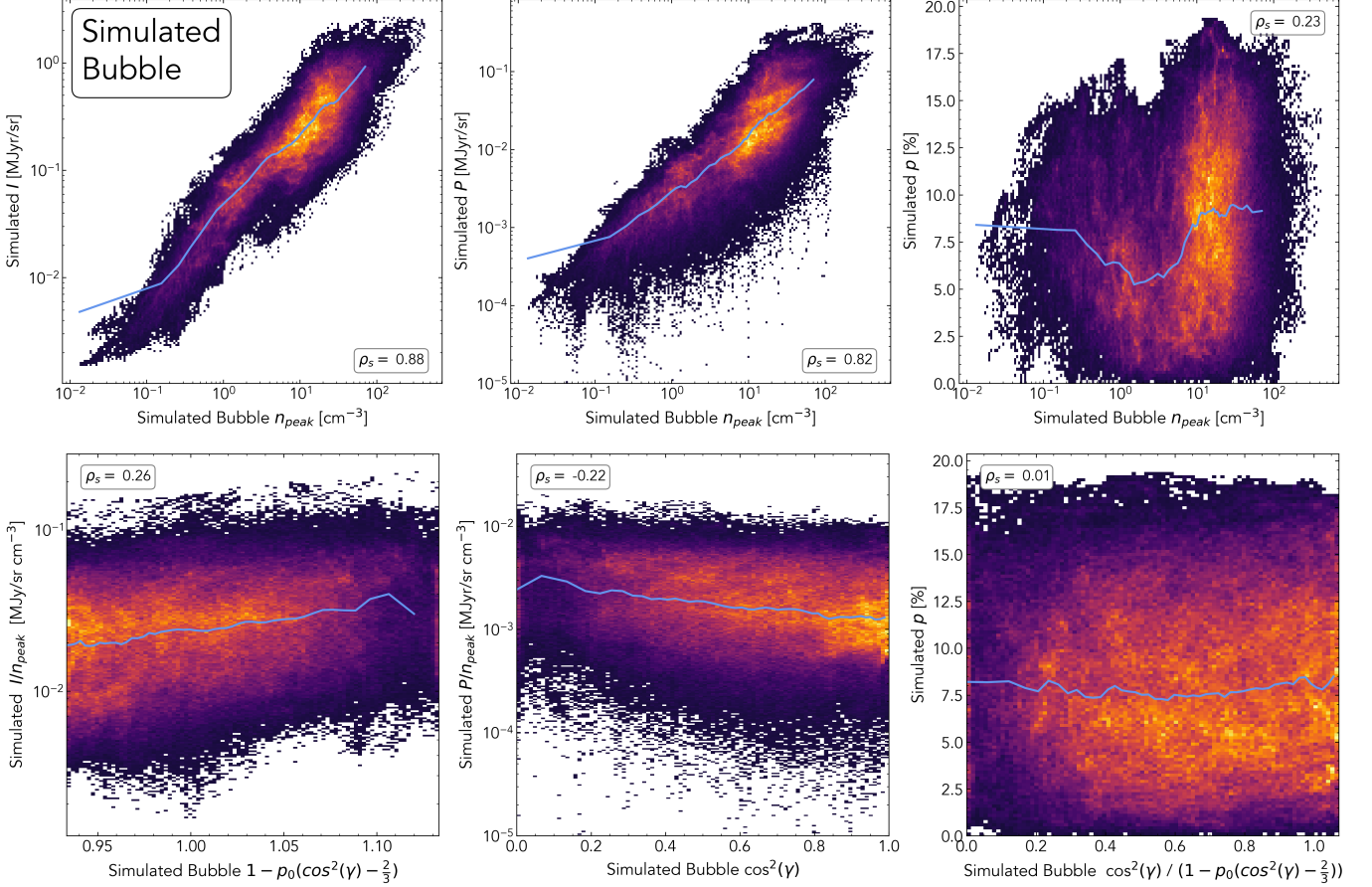


Figure B4. As Figure 3, but for correlations between the simulated bubble and simulated 353 GHz polarization metrics.

where reported uncertainties mark the 95% (2σ) credible intervals. The angular difference ($\cos^{-1}(|\hat{\mathbf{B}}_0 \cdot \mathbf{B}_0|)$) between our inferred $\hat{\mathbf{B}}_0$ and the true \mathbf{B}_0 is 3.9° . We deem this a successful reconstruction of the initial orientation of the simulated volume’s B-field. This suggests that our inference procedure is likely to yield a valid description of the initial orientation of the B-field in the

neighborhood on an evolved superbubble like the Local Bubble.

C. FITTING RESULTS FOR INITIAL LOCAL GALACTIC MAGNETIC FIELD

A corner plot showing the posterior distribution of θ inferred for the observed Local Bubble in §6 is shown in Figure C6.

REFERENCES

- Alves, F. O., Acosta-Pulido, J. A., Girart, J. M., Franco, G. A. P., & López, R. 2011, *AJ*, 142, 33
- Alves, F. O., & Franco, G. A. P. 2006, *MNRAS*, 366, 238
- . 2007, *A&A*, 470, 597
- Alves, F. O., Frau, P., Girart, J. M., et al. 2014, *A&A*, 569, L1
- Alves, J., Zucker, C., Goodman, A. A., et al. 2020, *Nature*, 578, 237
- Alves, M. I. R., Boulanger, F., Ferrière, K., & Montier, L. 2018, *A&A*, 611, L5
- Andersson, B. G., Lazarian, A., & Vaillancourt, J. E. 2015, *ARA&A*, 53, 501
- Andersson, B. G., & Potter, S. B. 2007, *ApJ*, 665, 369
- . 2010, *ApJ*, 720, 1045
- Andersson, B. G., Piirola, V., De Buizer, J., et al. 2013, *ApJ*, 775, 84
- Astropy Collaboration, Robitaille, T. P., Tollerud, E. J., et al. 2013, *A&A*, 558, A33
- Astropy Collaboration, Price-Whelan, A. M., Sipőcz, B. M., et al. 2018, *AJ*, 156, 123

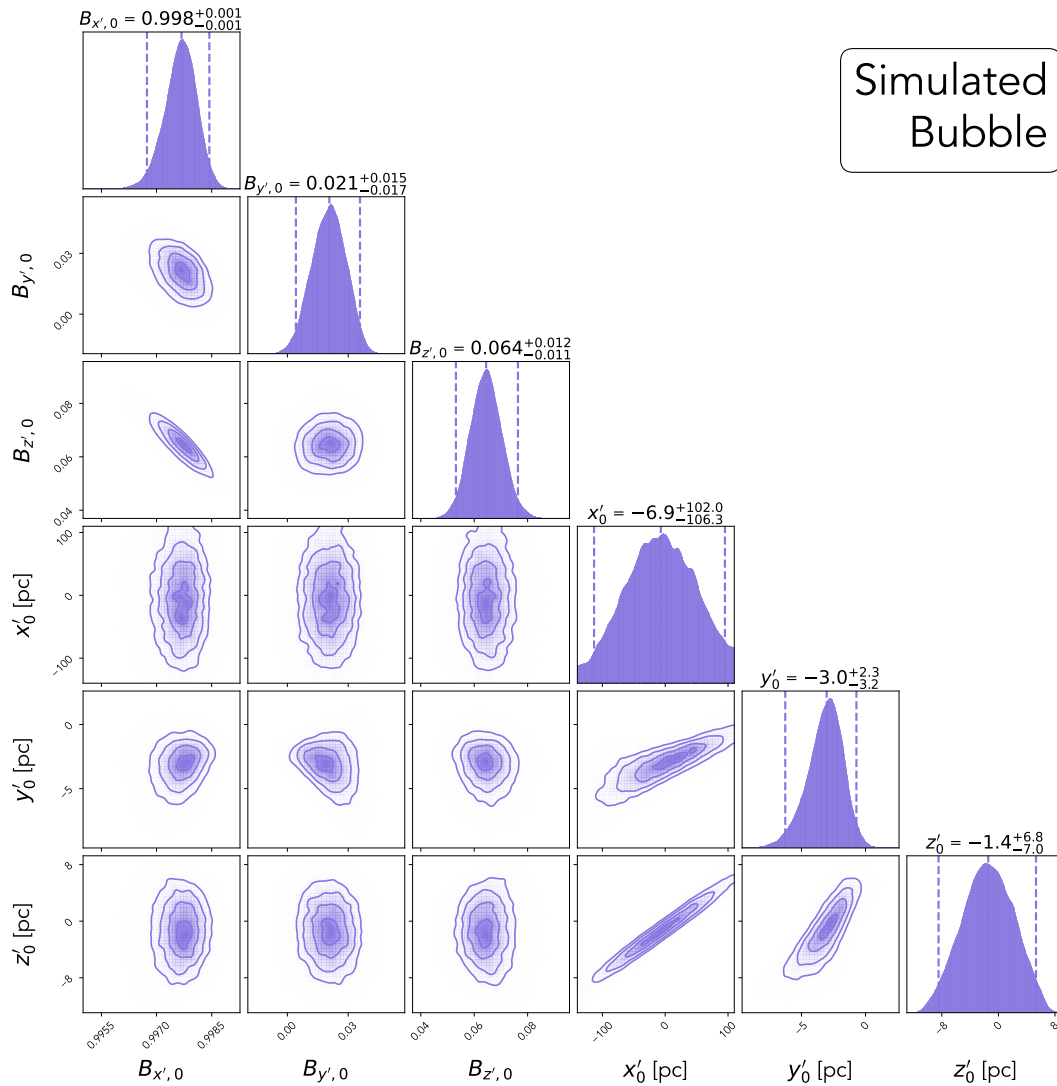


Figure B5. Corner plot showing the posterior distribution of θ for the simulated bubble. Reported uncertainties mark the 95% (2σ) credible intervals.

Astropy Collaboration, Price-Whelan, A. M., Lim, P. L., et al. 2022, *ApJ*, **935**, 167

Bailer-Jones, C. A. L., Rybizki, J., Fouesneau, M., Demleitner, M., & Andrae, R. 2021, *AJ*, **161**, 147

Bailey, J., Lucas, P. W., & Hough, J. H. 2010, *MNRAS*, **405**, 2570

Banerjee, A., Dhillon, I. S., Ghosh, J., & Sra, S. 2005, *Journal of Machine Learning Research*, **6**, 1345

Beck, R., & Wielebinski, R. 2013, *Magnetic Fields in Galaxies* (Dordrecht: Springer Netherlands), 641

Berdyugin, A., Piirola, V., & Teerikorpi, P. 2004, *A&A*, **424**, 873

—. 2014, *A&A*, **561**, A24

Berdyugin, A., & Teerikorpi, P. 2001, *A&A*, **368**, 635

—. 2002, *A&A*, **384**, 1050

Berdyugin, A., Teerikorpi, P., Haikala, L., et al. 2001, *A&A*, **372**, 276

Bijas, N., Eswaraiyah, C., Wang, J.-W., et al. 2022, *MNRAS*, **515**, 3352

Bock, A., Axelsson, E., Bladin, K., et al. 2017, *JOSS*, **2**, 281

Bracco, A., Bresnahan, D., Palmeirim, P., et al. 2020, *A&A*, **644**, A5

Cardelli, J. A., Clayton, G. C., & Mathis, J. S. 1989, *ApJ*, **345**, 245

Chakraborty, A., Das, H. S., & Paul, D. 2014, *MNRAS*, **442**, 479

Choudhury, G. B., Barman, A., Das, H. S., & Medhi, B. J. 2019, *MNRAS*, **487**, 475

Choudhury, G. B., Das, H. S., Medhi, B. J., et al. 2022, *RAA*, **22**, 075003

Cleveland, W. S. 1979, *JASA*, **74**, 829

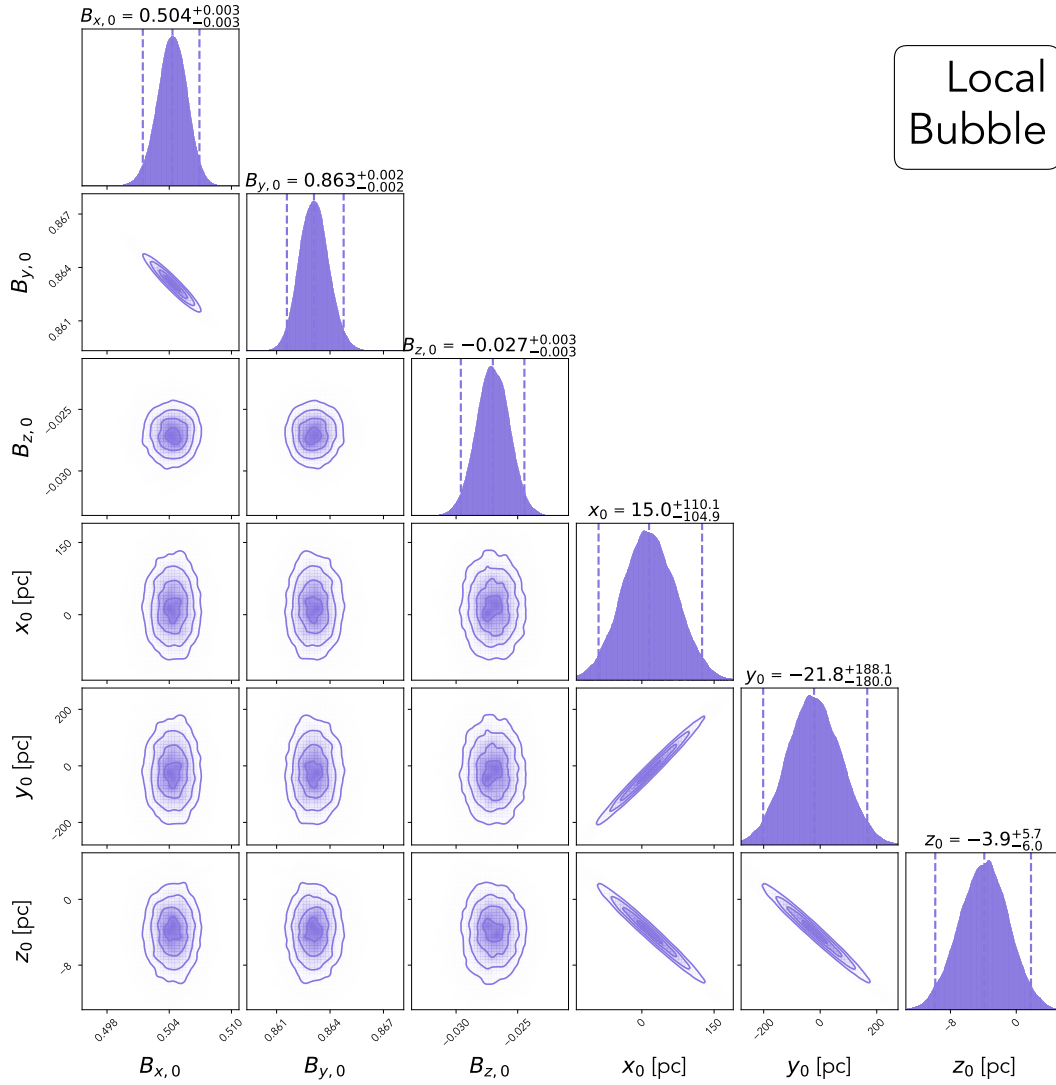


Figure C6. As Figure B5, but for θ sampled for the Local Bubble.

Cotton, D. V., Marshall, J. P., Bailey, J., et al. 2017, *MNRAS*, 467, 873

Cotton, D. V., Marshall, J. P., Frisch, P. C., et al. 2019, *MNRAS*, 483, 3636

Cox, D. P., & Reynolds, R. J. 1987, *ARA&A*, 25, 303

Das, A., Das, H. S., Medhi, B. J., & Wolf, S. 2016, *Ap&SS*, 361, 381

Dawson, J. R. 2013, *PASA*, 30, e025

de Avillez, M. A., & Breitschwerdt, D. 2005, *A&A*, 436, 585

Edenhofer, G., Zucker, C., Frank, P., et al. 2024, *A&A*, 685, A82

Elmegreen, B. G. 2011, in *EAS Publications Series*, Vol. 51, *EAS Publications Series*, ed. C. Charbonnel & T. Montmerle, 45

Eswaraiah, C., Maheswar, G., Pandey, A. K., et al. 2013, *A&A*, 556, A65

Eswaraiah, C., Pandey, A. K., Maheswar, G., et al. 2011, *MNRAS*, 411, 1418

Eswaraiah, C., Lai, S.-P., Ma, Y., et al. 2019, *ApJ*, 875, 64

Ferrière, K. 2016, in *JPhCS*, Vol. 767, *JPhCS* (IOP), 012006

Ferriere, K. M., Mac Low, M.-M., & Zweibel, E. G. 1991, *ApJ*, 375, 239

Fisher, R. 1953, *RSPSA*, 217, 295

Franco, G. A. P., & Alves, F. O. 2015, *ApJ*, 807, 5

Fuchs, B., Breitschwerdt, D., de Avillez, M. A., Dettbarn, C., & Flynn, C. 2006, *MNRAS*, 373, 993

Gao, X. Y., Reich, W., Reich, P., Han, J. L., & Kothes, R. 2015, *A&A*, 578, A24

Gil-Hutton, R., & Benavidez, P. 2003, *MNRAS*, 345, 97

Girichidis, P. 2021, *MNRAS*, 507, 5641

Girichidis, P., Seifried, D., Naab, T., et al. 2018, *MNRAS*, 480, 3511

- Girichidis, P., Walch, S., Naab, T., et al. 2016, *MNRAS*, 456, 3432
- Gontcharov, G. A., & Mosenkov, A. V. 2019, *MNRAS*, 483, 299
- Goodman, A. A., Bastien, P., Myers, P. C., & Menard, F. 1990, *ApJ*, 359, 363
- Górski, K. M., Hivon, E., Banday, A. J., et al. 2005, *ApJ*, 622, 759
- Green, G. M. 2018, *JOSS*, 3, 695
- Halal, G., Clark, S. E., & Tahani, M. 2024, *ApJ*, 973, 54
- Hamaker, J. P., & Bregman, J. D. 1996, *A&AS*, 117, 161
- Harris, C. R., Millman, K. J., van der Walt, S. J., et al. 2020, *Nature*, 585, 357
- Heiles, C. 1979, *ApJ*, 229, 533
- . 1996, *ApJ*, 462, 316
- . 2000, *AJ*, 119, 923
- Heyer, M. H., Vrba, F. J., Snell, R. L., et al. 1987, *ApJ*, 321, 855
- Higson, E., Handley, W., Hobson, M., & Lasenby, A. 2019, *Statistics and Computing*, 29, 891
- Hildebrand, R. H., Kirby, L., Dotson, J. L., Houde, M., & Vaillancourt, J. E. 2009, *ApJ*, 696, 567
- Hunter, J. D. 2007, *CSE*, 9, 90
- Joubaud, T., Grenier, I. A., Ballet, J., & Soler, J. D. 2019, *A&A*, 631, A52
- Keller, B. W., Wadsley, J., Benincasa, S. M., & Couchman, H. M. P. 2014, *MNRAS*, 442, 3013
- Konietzka, R., Goodman, A. A., Zucker, C., et al. 2024, *Nature*, 628, 62
- Krumholz, M. R., Bate, M. R., Arce, H. G., et al. 2014, in *Protostars and Planets VI*, ed. H. Beuther, R. S. Klessen, C. P. Dullemond, & T. Henning, 243
- Lee, H. M., & Draine, B. T. 1985, *ApJ*, 290, 211
- Leroy, J. L. 1999, *A&A*, 346, 955
- Linsky, J. L., & Redfield, S. 2021, *ApJ*, 920, 75
- Lobo Gomes, A., Magalhães, A. M., Pereyra, A., & Rodrigues, C. V. 2015, *ApJ*, 806, 94
- Maconi, E., Soler, J. D., Reissl, S., et al. 2023, *MNRAS*, 523, 5995
- Maíz-Apellániz, J. 2001, *ApJL*, 560, L83
- Mardia, K., & Jupp, P. 2000, *Directional Statistics*, Wiley Series in Probability and Statistics (Wiley)
- McKinney, W. 2010, in *Proc. 9th Python in Science Conf.*, ed. Stéfan van der Walt & Jarrod Millman, 56
- Medan, I., & Andersson, B. G. 2019, *ApJ*, 873, 87
- Medhi, B. J., Maheswar G., Pandey, J. C., Tamura, M., & Sagar, R. 2010, *MNRAS*, 403, 1577
- Moneti, A., Pipher, J. L., Helfer, H. L., McMillan, R. S., & Perry, M. L. 1984, *ApJ*, 282, 508
- Neha, S., Maheswar, G., Soam, A., & Lee, C. W. 2018, *MNRAS*, 476, 4442
- Neha, S., Maheswar, G., Soam, A., Lee, C. W., & Tej, A. 2016, *A&A*, 588, A45
- Ntormousi, E., Dawson, J. R., Hennebelle, P., & Fierlinger, K. 2017, *A&A*, 599, A94
- O'Neill, T. J., Zucker, C., Goodman, A. A., & Edenhofer, G. 2024, *ApJ*, 973, 136
- Oudmaijer, R. D., Palacios, J., Eiroa, C., et al. 2001, *A&A*, 379, 564
- Pandey, A. K., Eswaraiah, C., Sharma, S., et al. 2013, *ApJ*, 764, 172
- Panopoulou, G., Tassis, K., Blinov, D., et al. 2015, *MNRAS*, 452, 715
- Panopoulou, G. V., Dickinson, C., Readhead, A. C. S., Pearson, T. J., & Peel, M. W. 2021, *ApJ*, 922, 210
- Panopoulou, G. V., Hensley, B. S., Skalidis, R., Blinov, D., & Tassis, K. 2019a, *A&A*, 624, L8
- Panopoulou, G. V., Tassis, K., Skalidis, R., et al. 2019b, *ApJ*, 872, 56
- Panopoulou, G. V., Markopouloti, L., Bouzelou, F., et al. 2023, *arXiv e-prints*, arXiv:2307.05752
- Pelgrims, V., Ferrière, K., Boulanger, F., Lallement, R., & Montier, L. 2020, *A&A*, 636, A17
- Pelgrims, V., Panopoulou, G. V., Tassis, K., et al. 2023, *A&A*, 670, A164
- Pelgrims, V., Mandarakas, N., Skalidis, R., et al. 2024, *A&A*, 684, A162
- Pereyra, A., & Magalhães, A. M. 2002, *ApJS*, 141, 469
- . 2004, *ApJ*, 603, 584
- Pirola, V., Berdyugin, A., Frisch, P. C., et al. 2020, *A&A*, 635, A46
- Pineda, J. E., Arzoumanian, D., Andre, P., et al. 2023, in *ASPC, Vol. 534, Protostars and Planets VII*, ed. S. Inutsuka, Y. Aikawa, T. Muto, K. Tomida, & M. Tamura, 233
- Planck Collaboration, Ade, P. A. R., Aghanim, N., et al. 2015a, *A&A*, 576, A104
- . 2015b, *A&A*, 576, A105
- Planck Collaboration, Aghanim, N., Alves, M. I. R., et al. 2016a, *A&A*, 596, A105
- Planck Collaboration, Aghanim, N., Ashdown, M., et al. 2016b, *A&A*, 596, A109
- Planck Collaboration, Aghanim, N., Akrami, Y., et al. 2020a, *A&A*, 641, A3
- Planck Collaboration, Akrami, Y., Ashdown, M., et al. 2020b, *A&A*, 641, A4
- Planck Collaboration, Aghanim, N., Akrami, Y., et al. 2020c, *A&A*, 641, A12

- Plaszczynski, S., Montier, L., Levrier, F., & Tristram, M. 2014, *MNRAS*, **439**, 4048
- Poidevin, F., & Bastien, P. 2006, *ApJ*, **650**, 945
- Rand, R. J., & Kulkarni, S. R. 1989, *ApJ*, **343**, 760
- Reissl, S., Wolf, S., & Brauer, R. 2016, *A&A*, **593**, A87
- Remazeilles, M., Delabrouille, J., & Cardoso, J.-F. 2011, *MNRAS*, **418**, 467
- Robitaille, T., Beaumont, C., Qian, P., Borkin, M., & Goodman, A. 2019, glueviz v0.15.2: multidimensional data exploration
- Sandstrom, K. M., Koch, E. W., Leroy, A. K., et al. 2023, *ApJL*, **944**, L8
- Santos, F. P., Corradi, W., & Reis, W. 2011, *ApJ*, **728**, 104
- Santos, F. P., Franco, G. A. P., Roman-Lopes, A., Reis, W., & Román-Zúñiga, C. G. 2014, *ApJ*, **783**, 1
- Santos, F. P., Roman-Lopes, A., & Franco, G. A. P. 2012, *ApJ*, **751**, 138
- Sen, A. K., Gupta, R., Ramaprakash, A. N., & Tandon, S. N. 2000, *A&AS*, **141**, 175
- Serón Navarrete, J. C., Roman-Lopes, A., Santos, F. P., Franco, G. A. P., & Reis, W. 2016, *MNRAS*, **462**, 2266
- Silversmith, W. 2021, cc3d: Connected components on multilabel 3D & 2D images.
- Singh, S., Pandey, J. C., & Hoang, T. 2022, *MNRAS*, **513**, 4899
- Skalidis, R., & Pelgrims, V. 2019, *A&A*, **631**, L11
- Słowikowska, A., Krzeszowski, K., Żejmo, M., Blinov, D., & Reig, P. 2018, *MNRAS*, **479**, 5312
- Soam, A., Maheswar, G., Bhatt, H. C., Lee, C. W., & Ramaprakash, A. N. 2013, *MNRAS*, **432**, 1502
- Soam, A., Maheswar, G., Lee, C. W., et al. 2015, *A&A*, **573**, A34
- Soam, A., Maheswar, G., Lee, C. W., Neha, S., & Andersson, B. G. 2017, *MNRAS*, **465**, 559
- Soler, J. D., Bracco, A., & Pon, A. 2018, *A&A*, **609**, L3
- Speagle, J. S. 2020, *MNRAS*, **493**, 3132
- Stephens, I. W., Looney, L. W., Dowell, C. D., Vaillancourt, J. E., & Tassis, K. 2011, *ApJ*, **728**, 99
- Stil, J., Wityk, N., Ouyed, R., & Taylor, A. R. 2009, *ApJ*, **701**, 330
- Sullivan, C. B., & Kaszynski, A. 2019, *JOSS*, **4**, 1450
- Swiggum, C., Alves, J., D'Onghia, E., et al. 2022, *A&A*, **664**, L13
- Tahani, M., Plume, R., Brown, J. C., & Kainulainen, J. 2018, *A&A*, **614**, A100
- Tahani, M., Lupypciw, W., Glover, J., et al. 2022a, *A&A*, **660**, A97
- Tahani, M., Glover, J., Lupypciw, W., et al. 2022b, *A&A*, **660**, L7
- Tahani, M., Bastien, P., Furuya, R. S., et al. 2023, *ApJ*, **944**, 139
- Targon, C. G., Rodrigues, C. V., Cerqueira, A. H., & Hickel, G. R. 2011, *ApJ*, **743**, 54
- Tassis, K., Ramaprakash, A. N., Readhead, A. C. S., et al. 2018, *arXiv e-prints*, arXiv:1810.05652
- Thomson, A. J. M., McClure-Griffiths, N. M., Federrath, C., et al. 2018, *MNRAS*, **479**, 5620
- Tomisaka, K. 1998, *MNRAS*, **298**, 797
- Topasna, G. A., Jones, R. H., & Kaltcheva, N. T. 2020, *PASP*, **132**, 044301
- Trzesiok, A., tgandor, Kostur, M., et al. 2021, K3D-tools/K3D-jupyter: 2.11.0
- Vaillancourt, J. E., Andersson, B. G., Clemens, D. P., et al. 2020, *ApJ*, **905**, 157
- van der Velden, E. 2020, *JOSS*, **5**, 2004
- van Marle, A. J., Meliani, Z., & Marcowith, A. 2015, *A&A*, **584**, A49
- von Mises, R. 1918, *Physikalische Zeitschrift*, **19**, 490
- Vrba, F. J., Strom, S. E., & Strom, K. M. 1976, *AJ*, **81**, 958
- Walch, S., Girichidis, P., Naab, T., et al. 2015, *MNRAS*, **454**, 238
- Wang, J.-W., Lai, S.-P., Eswaraiah, C., et al. 2017, *ApJ*, **849**, 157
- Wardle, M., & Konigl, A. 1990, *ApJ*, **362**, 120
- Watkins, E. J., Barnes, A. T., Henny, K., et al. 2023, *ApJL*, **944**, L24
- Watson, G. S. 1965, *Biometrika*, **52**, 193
- Weitenbeck, A. J. 2008, *AcA*, **58**, 433
- Weitenbeck, A. J., Halstead, E. A., & Carver, A. J. 2008, *AcA*, **58**, 41
- Welsh, B. Y., & Shelton, R. L. 2009, *Ap&SS*, **323**, 1
- Whittet, D. C. B., Gerakines, P. A., Hough, J. H., & Shenoy, S. S. 2001, *ApJ*, **547**, 872
- Wisniewski, J. P., Bjorkman, K. S., Magalhães, A. M., & Pereyra, A. 2007, *ApJ*, **664**, 296
- Żejmo, M., Słowikowska, A., Krzeszowski, K., Reig, P., & Blinov, D. 2017, *MNRAS*, **464**, 1294
- Zhang, X., Green, G. M., & Rix, H.-W. 2023, *MNRAS*, **524**, 1855
- Zonca, A., Singer, L., Lenz, D., et al. 2019, *JOSS*, **4**, 1298
- Zucker, C., Goodman, A., Alves, J., et al. 2021, *ApJ*, **919**, 35
- Zucker, C., Goodman, A. A., Alves, J., et al. 2022, *Nature*, **601**, 334